PHYSICS OF OUR DAYS

PACS number: 96.50.Gn, 96.30.Kf

Collision of comet Shoemaker–Levy 9 with Jupiter: what did we see

V E Fortov, Yu N Gnedin, M F Ivanov, A V Ivlev, B A Klumov

Contents

Abstract. In July 1994, a dramatic event took place — the collision of the Shoemaker–Levy 9 comet with Jupiter. This collision has been accompanied by a great number of various effects in the atmosphere, ionosphere and magnetosphere of Jupiter. The comet impact became one of the most grandiose active experiments Nature has ever performed. Among the most interesting effects are bursts of radiation registered in a wide spectral range during the cometary fragments fall, the generation of giant gaseous plumes caused by the impact, the formation of large-scale long-lived vortex structures in the Jovian atmosphere. Unexpected events were the significant brightening of the Jovian radiation belts during the cometary fragments impact, the peculiarities of polar aurorae induced by the impact, the weakening of the Io plasma torus brightness observed in the extreme UV range, etc. In the present review, the results of the comet impact with Jupiter are discussed and a unified physical model is suggested which explains consistently the basic observational data.

V E Fortov, M F Ivanov, A V Ivlev High Energy Density Research Centre at Institute for High Temperatures, Russian Academy of Sciences, 13/19 Izhorskaya ul., 127412 Moscow, Russia
Tel. (095) 485-79-89
Fax (095) 485-79-90
E-mail: fort@hedric.msk.su, ivlev@hedric.msk.su
Yu N Gnedin Main Astronomical Observatory, Pulkovskoe Shosse 65/1 St-Petersburg, 196140, Russia
Tel. (812) 123-44-93
Fax (812) 123-19-22
E-mail: gnedin@pulkovo.spb.su.
B A Klumov Institute for Geosphere Dynamics, Russian Academy of Sciences, 36/6 Leninskiĭ prosp., 117334 Moscow, Russia
Tel. (095) 939-79-89
Fax (095) 137-07-11
E-mail: idg@glas.apc.org

1. Introduction

More than one and a half year has passed since the collision of the Shoemaker–Levy 9 (SL9) comet with Jupiter. This unique cosmic event, which we were happy to observe, occurs as rare as once per 1000 years. At present, the excitement caused by this event has somewhat decreased, and the time has come to tally some balance in order to understand what really happened on Jupiter in July 1994.

The importance of this review is also due to the fact that a lot of diverse observational data has been collected to date, which require the generalisation. The process of the impact has been observed by practically all largest observatories over the world, including the Hubble Space Telescope (HST), cosmic spacecrafts Galileo, Ulyss and Voyager. The observations were performed in a wide spectral range spanning from radio wavelengths to X-rays. The SL9 comet impact with Jupiter was accompanied by such a diversity of effects that it became extremely necessary to develop a unified physical model that would explain consistently the main observational data. In the present paper, we discuss the most significant and interesting, in our opinion, results of the encounter and in some cases suggest their interpretation. The main attention is given to those observational data that never will be revised. Such observations include, for example, the unique light curves of Jupiter obtained by cosmic spacecraft Galileo at the moments of some fragment impacts, the results of the HST observations of Jupiter in optical and UV bands, the ground based IR observations of Jupiter, the radio observations of the Jovian radiation belts during and after the collision. In the previous paper [1] we proposed a number of predictions relating to possible consequences of the SL9 comet colliding with Jupiter. Some of our predictions (such as the formation of long-lived vortex structures in the Jovian atmosphere caused by the fragment impacts and the estimate of their size, the radiation belts perturbations and the generation of artificial polar aurorae, the observed glow of metal ions, etc.) have been confirmed, but, as expected, the

nature of the collision proved to be much richer than any forecast, and the encounter of the SL9 comet with Jupiter gave us a number of bright and unexpected results, which are discussed in the present paper†. The comet impact became one of the most spectacular active cosmic experiments the Nature has ever performed, which probed different regions of the atmosphere, ionosphere and magnetosphere of Jupiter. In our opinion, it seems relevant to cite the list of the observed consequences of the SL9 impact, which we predicted and discussed in the paper 'Collision of comet Shoemaker–Levy 9 with Jupiter: what shall we see?' [1]:

"— the formation of long-lived vortex structures a few 1000 km in size in the Jovian atmosphere,

— the generation of optical flashes after the cometary fragment explosions,

— the generation of intrinsic gravitational waves by the raising cloud of explosion that stimulate condensation in the troposphere and form anomalies in the cloud cover,

— ionospheric and magnetospheric perturbations caused by the comet explosion,

— anomalies in radio emission from radiation belts of Jupiter, especially inside the magnetic force tubes crossing the impact site,

— features in the ionosphere and upper atmosphere glowing in optical, IR and radio bands."

Indeed, these effects proved the most prominent features of the SL9 impact with Jupiter, so we mainly discuss them in the present paper.

In Section 2 of the paper, we discuss observational data relating to the SL9 comet before and after its encounter with Jupiter, consider different hypotheses of its destruction and make different model evaluations of the size and density of the cometary fragments.

In Section 3, the processes occuring during the first half an hour after the impact are discussed: we analyze light curves of Jupiter taken on this time-scale in different spectral bands and suggest their explanation based on the model of strong explosion of the fragments in the inhomogeneous Jovian atmosphere.

In Section 4, we study long-term atmospheric perturbations caused by the cometary fragment impacts. We analyze data of spectroscopic observations of Jupiter obtained at late stages. Based on the data on atmospheric content of molecules synthesised during the fragment explosion, we estimate the size of the largest SL9 fragments. A typhoon model is suggested which allows us to explain the long-term evolution of the impact sites on time-scales from a few days to several months after the impact.

In Section 5, the principal effects caused by impact in the upper atmosphere, ionosphere and magnetosphere of Jupiter are discussed. Possible reasons for the radiation belt brightening in decimetre band, which were observed after the comet fragments fall, are considered. Mechanisms for exciting artificial polar aurorae are discussed.

It should be specially emphasised that this is only the beginning of detailed generalisations of the collision results.

---

† In this connection it is necessary to mention the historic mission of the Galileo spacecraft, whose probe entered dense layers of the planetary atmosphere on December 7, 1995. If the preliminary results obtained by the probe [2] (these data became known to the authors when the paper was in press) are confirmed by the subsequent processing, the current concepts on the structure and composition of the Jovian atmosphere should be revised.

2. The results of observations of the comet before its collision with Jupiter

The comet SL9 was discovered by american astronomers Caroline and Eugene Shoemaker and David Levy in March 1993. The early results of observations of the comet motion showed that a large enough probability existed that the comet would come across Jupiter. The results of the subsequent calculations of the comet orbit involving fresh data on its trajectory led to the conclusion that the encounter would be inevitable and would take place in July 1994. This became clear to the end of November 1993, after which a broad preparations had begun in order to observe the forthcoming event. All astronomical community worldwide was involved in this process under the supervision of the International Astronomical Union (IAU). Apart from ground-based observations, the comet was watched with the HST: the first images were taken on July 1, 1993, and beginning from January 1994, the observations were performed frequently enough until the SL9 fall on Jupiter. The reader may find a detailed list of the ground-based observatories and space-crafts which observed the collision in Ref. [3]. Table 1 contains the list of observatories (with observed objects indicated), from which observational data were used in the present review.

The comet comprised 25 separate cosmic bodies — radiating objects lined up in a chain a few million km in length. Fig. 1 shows the image of SL9 taken with the HST in May 1994 [4]. The trajectory calculations allow one to suggest that the objects constituting the comet in the image are the fragments of a large 'parent' cosmic body (see, e.g., Ref. [5]). According to these calculations, in the beginning of July 1992 the parent body already passed close to Jupiter at a distance of about $1.6R_J$ (R_J is the Jovian radius) and was destroyed by tidal forces caused by a strong gravitational field of Jupiter. Almost all researchers now agree with such a hypothesis for comet SL9 formation as a sequence of cosmic bodies. According to Ref. [6], the parent body was captured by Jupiter some decades ago, however, it is hardly possible to determine the parent body origin and its early trajectory due to the chaotic character of its orbit.

Much more unclear are attempts to answer the question as to what is the parent body from the point of view of morphology? Almost all present models consider the body consisting of discrete masses, and differ in the following: some authors believe that individual masses are connected with each other by a relatively weak mechanical coupling, whereas others think that the different fragments self-gravitate. As was noted in Ref. [7], this principal difference in the initial models goes back by some decades when two ideologically opposite models for cometary nucleus structure were put forward: a model of 'icy conglomerate' and a model of 'sand bank'. Essentially, the choice of the initial model for the SL9 parent body structure provides the opportunity to evaluate definitely the size and other characteristics of the luminous formations shown in Fig. 1. Putting aside the details, below we give only the conclusions from these models. A detailed description of the models can be found in an excellent monograph [8].

If the parent body were a conglomerate of a finite number of discrete nuclei connected mechanically with each other, their decay would proceed gradually [7]. During a fly-by of the parent body (with a size of about 10 km according to the 'ice conglomerate' model) near Jupiter in July 1992, the tidal

Table 1

Name of the observatory and telescope	Aperture of telescope	Method of observations	Object of observations
KECK, Mauna Kea, США	9.82 m	IR images	B, G, M, R fragments
Palomar, USA	5.08 m	IR images ($\lambda =2$–4 μm) spectrometry ($\lambda =8$–14 μm)	A, B, C, E, F, G1, H, K, L, Q, R, S, U, V, W
Anglo-Australian telescope (AAT), Australia	3.9 m	Near IR images, spectroscopy, fast photometry	A, C, D, E, G, H, K, L, N, Q, R, S, V
European Southern Observatory (ESO), La Silla, Chili	3.6 m 3.5 мм-New Technology Telescope (NTT) 2.2 m	Middle, far IR images, IR spectroscopy (2–3 μm)	A, B, C, D, E, F, G, H, K, L, Q, R, S, T, U, V, W
Calar Alto, Spain	3.50 m 2.20 m 1.20 m	Fast IR photometry, IR images	A, C, D, E, G, H, L, P2, Q, S, T, U, V, Europa satellite
Hubble Space Telescope (HST)	2.4 m	Images at different wavelengths ranged from IR to UV, UV spectroscopy	A, B, C, D, E, F, G, H, K, L, N, Q, R, S, W
Pic du Midu, France	2.0 m 1.0 m	Optical, IR images, optical, IR spectroscopy	A, B, C, D, E, G, H, K, L, N, P2, Q1
Galileo spacecraft,	Photopolarimeter-Radiometer, Near-Infrared Mapping Spectro-meter NIMS, Solid State Imager SSI, UV Spectrometer, UVS	$\lambda =945$ nm $\lambda =1.5$–4 μm $\lambda =890$ nm $\lambda =290$ nm	Entry of fragments G, H,L, R, K, W, Q1, N into the atmosphere of Jupiter
Australian radiotelescope (AT), Australia		Radioemission in decimetre diapason ($\lambda = 13$ cm, 22 cm)	Jovian radiation belts
Extreme UV explorer satellite (EUVE)		Extreme UV emission ($\lambda \simeq 300\,\text{A} - 800\,\text{A}$)	(Io plasma torus –IPT)
International Ultraviolet Explorer satellite (IUE)		UV emission $\lambda \simeq 1700\,\text{A} - 2300\,\text{A}$	(Io plasma torus –IPT)

Figure 1. The image of the SL9 comet taken by the HST in May 1994. Each fragment of the comet is labelled with a letter.

Table 2

Fragment	A	B	C	D	E	F	G₂	G₁	H	K	L	N	P2	P1	Q2	Q1	R	S	T	U	V	W
Diameter km	1.4	1.7	2.1	1.4	2.8	2.1	0.8	4.0	3.0	3.8	3.5	1.4	0.85	3.0	3.0	4.0	2.5	2.9	0.64	0.9	1.35	2.4
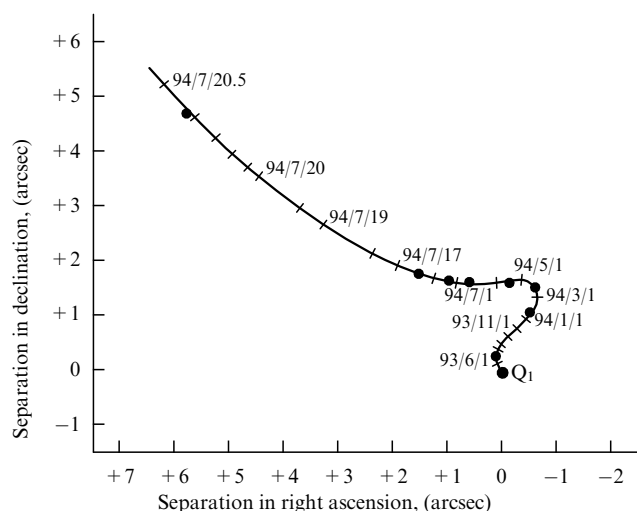
Figure 2. Reciprocal position of Q1-Q2 fragments at different moments of time. Observational data taken by the HST (•) and the results of an optimized solution based on the 'ice conglomerate' model [7] are presented.

forces led to its cracking and decay into several large fragments (two or three most probably), which continued decaying already after the perigee passage. The secondary fragmentation continued for a sufficiently long time, at least until April 1993. This conclusion follows from the comparison of observational data on reciprocal positions of fragments in complexes Q1–Q2 with results of calculations (Fig. 2 from Ref. [4]). As a result of the secondary fragmentation, the parent body decayed ultimately into a large enough number of fragments with sizes from a few hundred meters to $2 - 3$ km. Subsequently, under the action of the gravitational field gradient, these fragments lined up along a straight line.

In case the parent body were a collection of small (with a size of about 100 m and below) nuclei (the 'sand bank' model) holding together by the self-gravitation (Refs [9, 10]), the fragmentation would proceed quite differently. In this case, the characteristic size of the parent body was about 1.5 km, which is significantly less than in the previous model. By approaching Jupiter, the nuclei of the parent body with such a structure is stretched up by the planet's gravitational field in the direction toward the Jupiter centre. Then, as going away from Jupiter, the process of a reverse fragmentation begins in the 'string' consisting of small-size fragments and dust. This process develops due to a peculiar gravitational collapse that leads to the appearance of several 'centres of condensation' inside the 'string'. Ultimately, this process leads to the 'string' decay into two-three tens of the centres, each of which, in turn, comprises up to several ten of small fragments. According to this model, these are the centres that we see in Fig. 1.
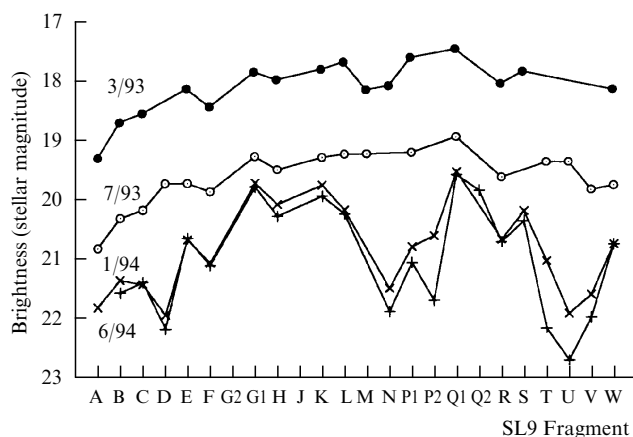
In spite of the successful explanation the latter models offer for the fragmentation process of the parent body, the first model seems to be more preferable for the following reasons. Firstly, the results obtained in Ref. [9, 10] (the number of the condensation centres', the length of the 'chain', etc.), as the authors note themselves, prove to be very strongly dependent on both the average density of the parent body and its spin angular velocity. In other words, a small enough change in any of these parameters leads to a

qualitative change in the solution obtained and makes impossible the process development according to the scenario given above. Secondly, the 'sand bank' model can not, in principle, explain the secondary fragmentation of the parent body a half a year later the fly-by near Jupiter, whereas the conclusion about fragments decay extremely prolonged in time is a natural consequence from the models considered above. Thirdly, this model offers a correct prediction for the effects that accompanied the comet approaching to Jupiter and its fall in July 1994. According to this model, one could expect a significant growth in size of the luminous formations (not only of the outer but also of the inner coma!) in the direction toward Jupiter's centre when approaching it; in addition, the fall of small fragments of the order of 100 km in size could not lead to the consequences that were observed during impact of many fragments (we discuss this point in detail below). Along with the determination of the cometary nucleus structure, the similar number of questions is posed by an attempt to determine its chemical composition and to find whether the SL9 is actually a comet or we rather deal with an asteroid. On the one hand, the results of measuring the colour of the inner coma of individual fragments show that the dust that forms the inner coma, had a colour either a slightly more red [4], or the same [11] as the solar light, which is characteristic of the cometary dust. On the other hand, such colour of the coma is typical also for wide-spread types C and S of asteroids. In addition, spectral observations of the SL9 have not revealed the expected emission at the wavelength 3090 A corresponding to the strongest band (0–0) of the hydroxide radical OH, which is present in the coma of practically all comets observed within a distance of about one astronomical unit (AU) from the Sun [4]. No variability in the bands corresponding to the emission from molecules CS and CO_2^+, typical for comets, have also been observed. The absence of emission from the OH radical does not exclude at all the possibility that the SL9 fragments consisted of ice or, in general, that water was present in the SL9 material. The point is that the SL9 was at a significant (more than 5 AU) distance from the Sun and, hence, the surface of its fragments could have a too low temperature, so the amount of water evaporated per unit time could well be insufficient for the OH radical emission to be detected on Earth. But then the absence of emission from CS and CO_2^+ remains unclear, since these molecules arise from CS_2 and CO_2 which, in turn, are much more volatile than water. The amplification of emission in the region of the CN (0–0) band at the wavelength 3785 A has not also been detected. This allowed the evaluation of the upper limit for the CN production rate, which for different fragments turned out to be close to the values obtained for other periodical comets, such as Howell and Haneda–Campos 1978J [12]. The presence of coma in the SL9 evidences for its cometary origin. However, the absence of gas emission usually observed in comets is typical for asteroids, especially because asteroids can be surrounded by a dust coma.

In other words, a definite answer to the question as to whether we deal with a comet or an asteroid in this case, is hardly possible. In what follows, owing to the historical tradition, we shall refer to the SL9 as comet.

The Hubble Space Telescope observations of the SL9 have provided an opportunity to evaluate the motion of individual fragments relative to each other and to determine their coma emission brightness at different time. In addition, these observations allow one to determine the relative size of the
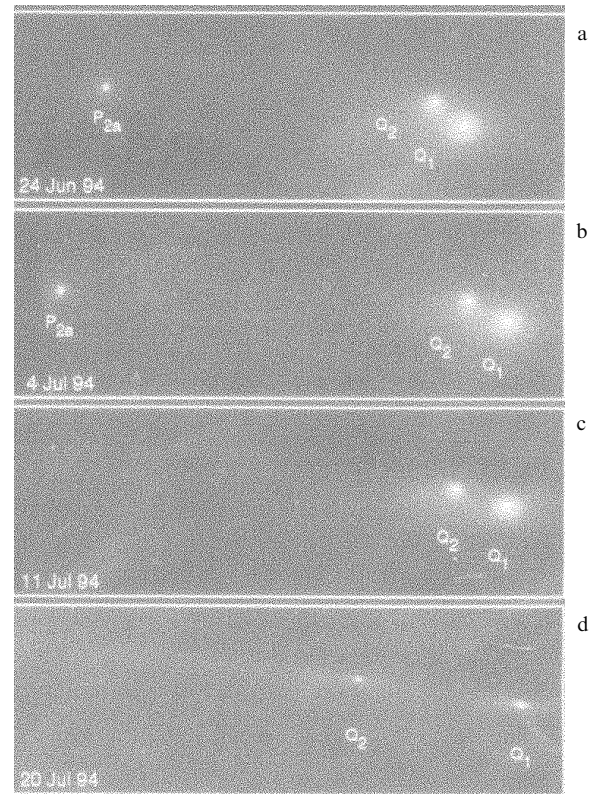
fragments, as well as to estimate their absolute dimensions. During the total period of tracing the comet beginning on July 1st 1993, the distance between fragments A and W five times decreased [4]. During the same period of time, the brightness of each fragment decreased on a characteristic time-scale of about a month (Fig. 3 from Ref. [13]), which resulted from the dispersion of the dust forming the coma. According to estimates [4], the mass of the dust coma was of the order of 10^{10} g for a typical SL9 fragment. During the time of observations, the decay of some fragments (Q1–Q2, G1–G2, P2a–P2b) was discovered; this process was already described above as a secondary fragmentation. In the sequence of images showing the relative position of fragments Q1, Q2 and P2a at different moments of time (Fig. 4 from Ref. [4]), the process of their mutual receding is clearly seen. The main feature of the fragments resulted from the secondary frag-mentation is that they were located somewhere apart from the line passing through the fragments existing earlier, and the process of their brightness decrease went much faster (probably because the 'young' fragments possessed more dust in the surrounding coma). In the next Section we return to discussing properties of these fragments in connection with the fact that the observational effects, which accompanied the fragments fall, were somewhat different from what was observed during the fall of 'old' fragments of the comet.

Figure 4. Reciprocal position of P2a, Q1, and Q2 fragments at different moments of time. The image was taken by the HST [4].

Figure 3. Relative brightness of the SL9 fragments at different moments of time.

As is seen from Fig. 1 and 4, the inner coma of each fragment had a round form with a radius of about 2000 km, with the cometary tail being directed out from the Sun. This evidences that the tail formation was determined not only by the action of the gravitational field and solar radiation, but also by some other factors, for example the Jovian magnetic field. The coma of each fragment preserved the round shape until about two weeks prior to the collision with Jupiter, after which the outer coma experienced rapid stretching in the direction toward Jupiter: apparently, this process was caused by the action of the increasing gradient of gravitational field. While the outer coma stretched up by more than 10 times to the moment of fragments impact (see the last image in Fig. 4), the inner coma preserved its round form, which points to the absence of the fragmentation during the approach to Jupiter, predicted in Refs [9, 10].

Using the iterative deconvolution technique, relative brightness of each fragment was calculated and its size was determined [14]. These estimates were done by assuming a power-law dependence of the coma emission intensity on radius. The results of these calculations are listed in Table 2, therefrom it follows that the size of nucleus of the largest fragments does not exceed 3 – 4 km. Photometric observa-tions of each of the fragments revealed no evidence for their possible spin or precession.

3. Observations during the comet impact with Jupiter

The time and sites of impact of the SL9 comet fragments on the Jovian surface were calculated by many authors (see, for example, Refs [15, 16]). According to their calculations, the A fragment was to collide with Jupiter on July 16, and two last V and W nuclei — on July 22. Based on these data, in the second decade of July a large number of ground-based telescopes at different sites on Earth began observations. Observatories located in the southern hemisphere had the best opportunities for observations of Jupiter (its visibility from a given point, as well as weather conditions). Especially favourable weather conditions were at observatories of South Africa (SAAO) and Australia (AAT). A rather long series of observations were obtained at La Palma (Canary Islands), Calar Alto (Spain), observatories of Japan and Hawaii Islands.

In spite of bad weather, a significant contribution to observations of this unique event was made by European Southern Observatory (ESO) located in Chile. Ten telescopes were involved in the observations, among which were large telescopes with a mirror diameter of 3.5 m and 3.6 m (the so-called New Technology Telescope, NTT, using new principles of adaptive optics). A high-sensitive infrared detector

TIMMI worked most effectively by allowing one to obtain images in the far IR region. This device operated successfully even in the day-time. As a result, using the NTT telescope (ESO) and TIMMI detector, more than 120 000 images of the impact sites of the comet fragments, as well as light curves of Jupiter during the fall of SL9 nuclei, were obtained, and the temporal evolution of the sites was studied.

An extremely important observational data was obtained with the Hubble Space Telescope. Observations performed by this instrument provided detailed images and spectral measurements of atmospheric phenomena caused by the fragments impact. A valuable contribution for understanding the processes caused by the cometary fragments encounter was made by analyzing the data obtained by the Galileo spacecraft, as the impact sites on the Jupiter surface were directly seen by the Galileo, whereas for terrestrial observers they were on the dark side of Jupiter. Fig. 5 depicts the reciprocal position of Earth, Jupiter, the Galileo and Sun in July 1994. Observations were performed with the following four instruments: the Near-Infrared Mapping Spectrometer (NIMS), the Photopolarimeter-Radiometer (PPR), the Solid State Imager (SSI) and the Ultraviolet Spectrometer (UVS). Observations carried out with these instruments in a wide spectral range from IR to UV enabled one to get various information (brightness, colour, polarisation, etc.) about processes occurring in the Jovian atmosphere just after the comet fragments impact.
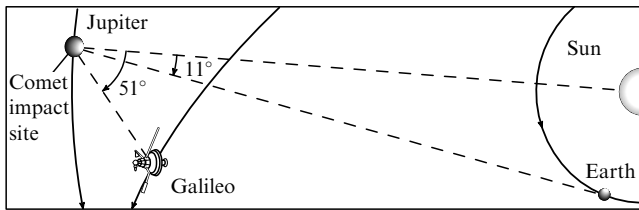
**Figure 5.** Reciprocal position of Earth, Jupiter, Sun, and the Galileo spacecraft in July 1994.

Below we discuss in detail the main observational results obtained during first tens minutes after the fragments collision with Jupiter, and try to bind the most reliable effects observed in a single physical picture.

3.1 Jupiter observations during impacts: the data obtained by the Galileo spacecraft

Observations of Jupiter during fragments impact were performed at different wavelengths including IR (1.84 – 4.38 μm, NIMS), near IR and visible light ($\lambda = 890$ nm and 945 nm, PPR, and $\lambda = 890$ nm and 560 nm, SSI), as well as in the UV-region ($\lambda = 292$ nm, UVS). The impact of many fragments was accompanied by bursts of radiation which were detected by the Galileo. Fig. 6 – 8 show light curves obtained at different wavelengths with the PPR [17], NIMS [18] and SSI [19]. The data presented are a small portion of the results obtained by the Galileo during the whole period of observations; nevertheless, characteristic features of these results are clearly seen in the plots presented. First, the most prominent is a sharp increase in the radiation intensity during the first 1 – 2 s from the background level to a maximum. This feature is typical for almost all light curves obtained by the Galileo (excluding some curves taken with NIMS in the IR band, see Fig. 7b). Subsequent behaviour of the light curve
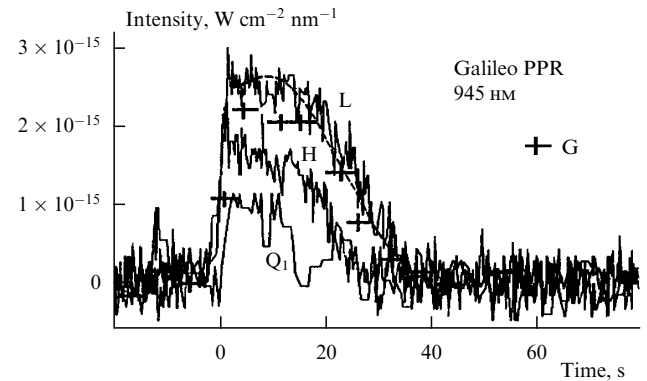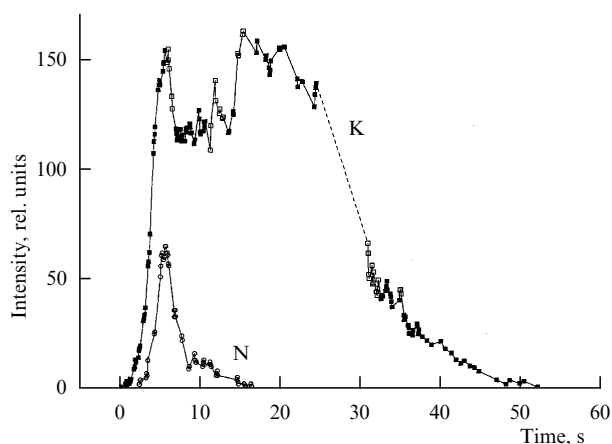
Figure 6. Light curves obtained by the Galileo spacecraft (with the PPR device) for some impacts [17] at the wavelength $\lambda = 945$ hm. The dashed curve corresponds to the analytical solution (7).
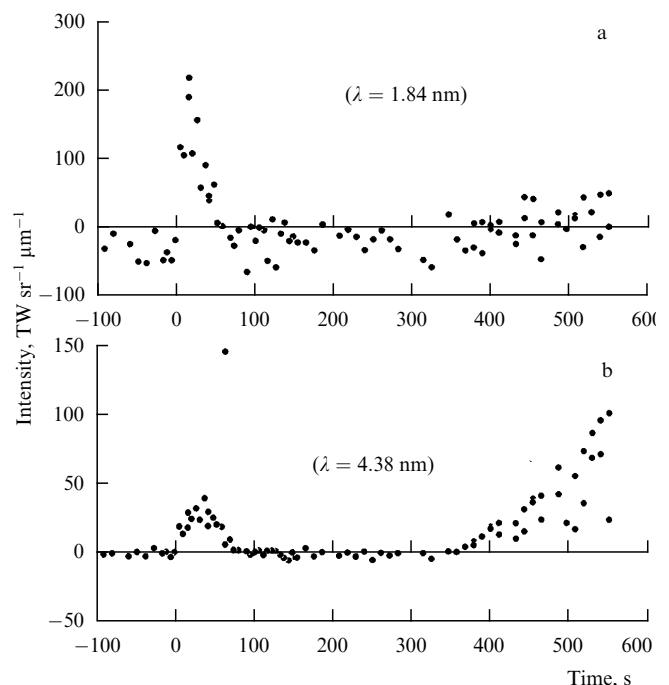
Figure 7. Light curves obtained by the Galileo spacecraft (with the NIMS device) for the G fragment impact [18] at the wavelength $\lambda = 1.84$ μm (a) and $\lambda = 4.38$ μm (b).

turns out to be strongly wavelength-dependent. In addition, the behaviour of light curves obtained for some fragments at the same wavelength differs significantly from that of all other fragments.

Temporal dependencies of the emission intensity obtained with the PPR (Fig. 6) for different fragments are identical in shape to each other, whereas the higher the maximum intensity of the bursts, the longer their durations are. After the sharp intensity increase, a specific 'plateau' with a duration of 10 – 15 s appears, after which a more smooth, nearly linear decrease down to the background level begins. The total duration of emission is 30 – 40 s for different fragments, except for the Q1 fragment light curve. This curve shows at least four clear outbursts of emission. The light curves obtained with the NIMS (Fig. 7) have lower temporal resolution, but the general form of the NIMS light curve is the

Figure 8. Light curves obtained by the Galileo spacecraft (with the SSI device) for some impacts [19] at the wavelength $\lambda = 0.89\ \mu m$.

same as of the PPR light curve. The comparison of maximum emission intensities taken at different wavelengths enabled the authors [17] to evaluate a temperature of radiation as of order 10000 K.

The NIMS measurements (Fig. 7) revealed the increase in the emission intensity registered about six minutes after the first outburst. It is especially important to note that the time interval between the first maximum and the beginning of this increase is of about 6 – 7 min for all curves registered by the NIMS [18]. The comparison of light curves at different wavelengths permits one to conclude that the temperature of the first outburst far exceeds the temperature of the radiation whose intensity was registered to increase to the end of the light curve from Fig. 7b.

A special place is taken by the SSI data obtained at a wavelength of $\lambda = 0.89\ \mu m$ (Fig. 8). After a sharp increase in the radiation intensity, an equally strong decrease begins. Then this drop is accompanied by either some decrease in intensity during 10 – 15 s (fragment K) after which the light curve tends to the initial intensity level and behaves subsequently similar to the case of the PPR light curve, or the fast drop leads to the emission decrease down to the background level for a short time interval of less than 10 s. Such a behaviour of light curves was discovered for fragments N and W impacts (in the latter case the measurements were done at a wavelength $\lambda = 0.56\ \mu m$). An explanation for such a strange behaviour of light curves is given in Section 3.3.

3.2 Jupiter observations during impacts:
the data obtained on Earth and by near-Earth spacecrafts
In this section we present the results of observations obtained on Earth during about half an hour after each comet fragment collision with Jupiter. All other 'later' results are considered in Sections 4 and 5. Such a subdivision of data by 'early' and 'late', and the phenomena on Jupiter corresponding to them by 'fast' and 'slow', is, of course, conditional, but we will use such a classification because these phenomena occur on significantly different time scales.

We start to describe 'fast' processes that were registered on Earth or by spacecrafts in close-to-Earth orbits with listing the HST data. The images taken with this telescope are primarily interesting in having an extremely good resolution to see in detail atmospheric processes (both 'fast' and 'slow')

that accompanied the fragments impact. The information provided by these images is very important in allowing us to estimate, both qualitatively and quantitatively, the processes occurring on Jupiter.

One of the most impressive results obtained by the HST is images of luminous features that arose above the Jupiter limb shortly after the fall of many large fragments, whereas the impact site itself is on the dark side of the planet and is not yet seen from Earth. These features are usually referred to as 'plumes' or 'ejecta'. Since the HST observations did not cover the impact time for all fragments, only four series of images were obtained, which are presented in Fig. 9. Table 3 lists the wavelength, exposure duration and time for each frame. Each of these series demonstrates the evolution of the ejection appeared after the impact of one of the fragments (A, E, G, and W). In total, the ejection appearance was discovered after the fall of ten largest nuclei [20], which enables us to reconstruct a sufficiently complete picture of this phenomenon and to consider the ejection as a typical effect that accompanies the impact. Impacts of small-size fragments did not lead to somehow noticeable observational consequences,

Table 3

| Image	Wavelength, nm	Exposure time, s	Time, UT
		A	
1	890	14	20 : 13
2	890	4	20 : 15
3	953	16	20 : 18
4	547	0.16	20 : 21
5	410	2	20 : 24
6	336	3.5	20 : 27
7	890	4	20 : 30
8	953	16	20 : 33
		E	
1	890	30	15 : 19
2	890	16	15 : 21
3	953	35	15 : 24
4	555	0.3	15 : 27
5	410	10	15 : 30
6	336	18	15 : 33
7	255	300	15 : 39
8	890	30	15 : 49
9	953	35	15 : 52
		G	
1	890	100	7 : 30
2	890	30	7 : 33
3	890	16	7 : 35
4	953	16	7 : 38
5	555	0.3	7 : 41
6	410	10	7 : 44
7	336	18	7 : 51
8	890	100	7 : 55
9	890	30	7 : 58
		W	
1	890	100	7 : 55
2	890	30	7 : 58
3	890	16	8 : 00
4	953	16	8 : 03
5	555	0.3	8 : 06
6	410	10	8 : 09
7	336	18	8 : 16
8	890	100	8 : 20
9	890	30	8 : 23

3000 km
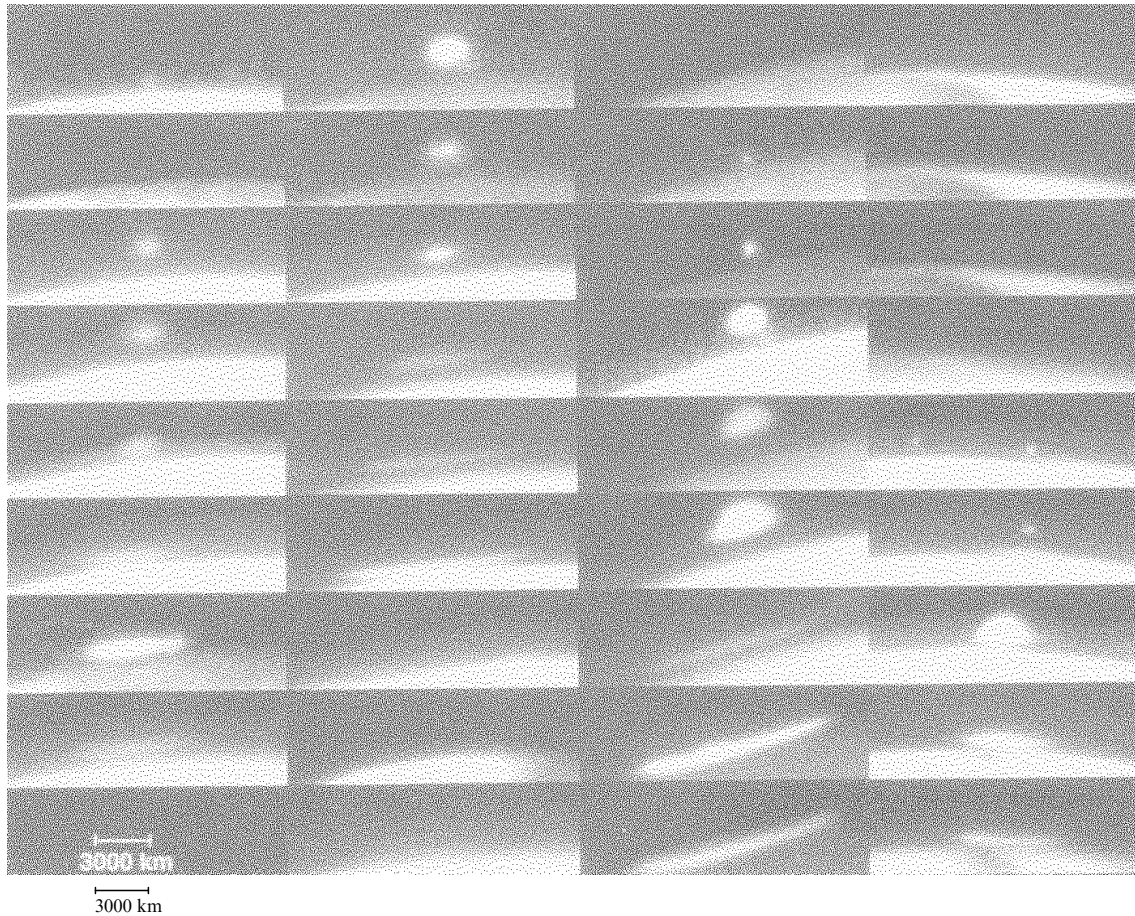
Figure 9. Series of images of ejecta formed during the A,E,G,W fragment falls. The images were taken by the HST [50]. Characteristics of each image (exposure time, observational wavelength, and the corresponding time) are listed in Table 3.

therefore below we focus on the effects caused by large fragments more than one km across. The series of images of the ejection appeared after the G fragment impact (the third series in Fig. 9) demonstrates clearly all main stages the ejection passed in most cases. First, a short outburst appeared with a duration less than one minute (2nd frame), followed by some decrease of the glowing. Then, the luminous spot above the limb got gradually larger during 4 – 5 min (3nd frame), after which its growth in size became much faster. The luminous ejection attained a size of some tens thousand km (4th, 5th and 6th frames), and the altitude above the limb it rose was about 3000 km (Fig. 10). After other 5 – 7 min the spot of ejection became decreasing in size and after about 10 min disappeared completely. At the same time, at altitudes of 200 – 300 km above the limb an extended, relatively weakly shining belt (7th frame) appeared, which corresponded to enormous, bright in methane bands, spots (see Table 3) that arose on the Jovian surface after the impact sites had turned to be seen from Earth. We give a description of these spots and discuss their possible nature in Section 4.

Observations of the fragment impact time done with ground-based telescopes allow the construction of a variety of light curves in the visible and IR bands. Fig. 11 shows the light curves taken at $\lambda = 2.3$ μm, 3.2 μm and 4.5 μm with telescopes at Palomar Observatory [21] (Fig, 11a, b) and Mauna Kea Observatory [22] (Fig, 11c) during the R fragment fall. These light curves are typical in the sense that

they contain all common features with other light curves. The first outburst of emission (Fig. 11b) was relatively weak and very short, its duration was less than a few tens of seconds. After the first outburst, the second, much stronger one followed in many light curves (but not in all!), whose intensity far exceeded the background level. A feature of the second
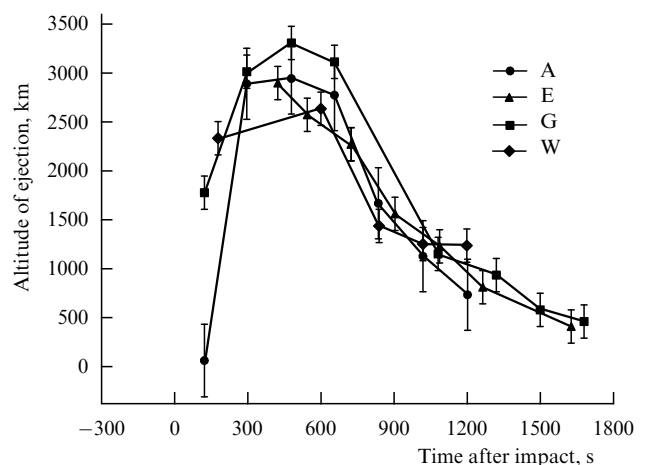
Figure 10. The time dependence of the altitude reached by the ejections caused by A, E, G, W fragment impacts [50].
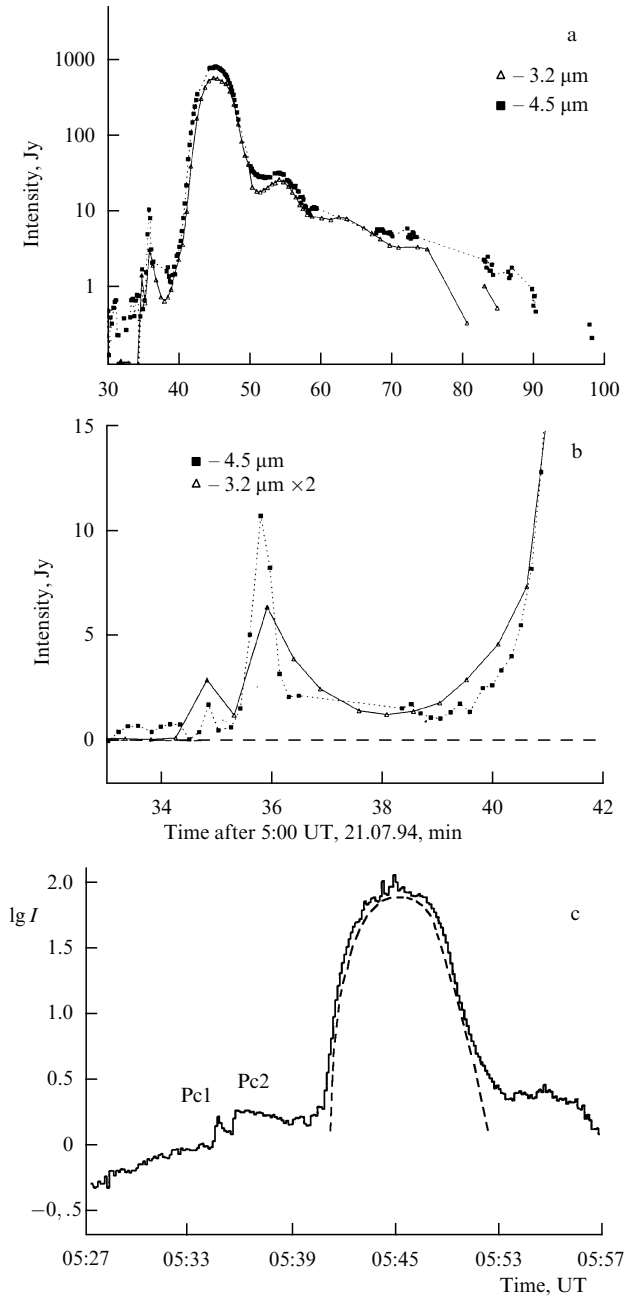
Figure 11. (a) Light curves obtained at the Palomar observatory during the R fragment impact at different wavelengths [21]: $\lambda = 3.2$ μm and $\lambda = 4.5$ μm; (b) the detailed structure of the Pc1 and Pc2 precursors at two wavelengths: $\lambda = 3.2$ μm and $\lambda = 4.5$ μm; (c) light curves obtained at the Mauna Kea observatory during the R fragment impact at the wavelength $\lambda = 2.3$ μm [22]. The dashed line corresponds to the analytical dependence (10). 1 Jy $= 10^{-26}$ W m^{-2}Hz^{-1}.

outburst is that the shorter the wavelength of observation, the longer the outburst duration and the lower its intensity are (Fig. 11b). So at short wavelengths the second outburst had a plateau-like form , i.e. after the sharp increase the intensity varied rather weakly with time. For example, at the wavelength $\lambda = 2.3$ μm (Fig. 11c) after reaching the second maximum in the light curve, the intensity decreases only one and a half times during four minutes, i.e. the term 'outburst' is not strictly appropriate in this case. So in the literature it is accepted to term the first two maxima as 'precursors', or briefly Pc1 and Pc2. About five minutes after the Pc1

emerging, the intensity of radiation begins rapidly increasing, which indicates the beginning of the so-called 'main event' in the light curve (Fig. 11a, c). It should be noted that the time interval between the Pc1 appearing and the main event beginning is of about $5 - 6$ min almost for each of the light curves obtained. The main event duration in the typical light curve is of the order of ten minutes, after which a 'plateau' appears in the curve. The duration of this 'plateau', as well as its intensity (relative to the main event), varies strongly depending on wavelength and fragment. For example, the 'plateau' intensity in the H fragment light curve ($\lambda = 10$ μm) is some tenth of the main event intensity, whereas the 'plateau' in the R fragment light curve ($\lambda = 2.3$ μm) has the relative intensity an order of magnitude lower.

Table 4

Fragment	Moment of registration of the first impact (UT) with indication of wavelength and exposure time		Time delay between the ground-based and satellite observations, s
	ground-based observatory	HST and Galileo	
		18 July	
G	7 : 32 : 58 (AAT 2–2.4 μm 3 min)	7 : 33 : 15 (HST 890 nm 30 s) 7 : 33 : 32 (Galileo PPR 945 nm, 5 s) 7 : 32 : 37 (Galileo NIMS 1.5 μm, 5 s)	$\gtrsim 40$
		18 July	
H	19 : 30 : 42 (Pic du Midi 2 μm, 3 s) 19 : 31 : 45 (Calar Alto (2.3 μm, 20 s)	19 : 31 : 58 (Galileo PPR 945 nm, 5 s)	$\gtrsim 15$
		19 July	
K	10 : 22 : 42 (AAT, 2–2.4 μm, 40 s)	10 : 24 : 13 (Galileo SSI 890 nm, 5 s)	$\gtrsim 10$
L	22 : 16 : 32 (Calar Alto 2.3 μm, 3 s) 22 : 16 : 35 (Pic du Midi 2 μm, 3 s)	22 : 16 : 48 (Galileo PPR 945 nm, 5 s)	$\simeq 5$
R	5 : 34 : 45 (Keck, 23 mm, 7.7 s) 5 : 34 : 50 (Palomar, 3.5 μm, 8 s) 5 : 34 : 52 (Palomar 4.5 μm, 8 s)	5 : 35 : 19 (Galileo NIMS 1.5 μm, 10 s)	$\simeq 30$
W	8 : 06 : 56 (AAT, 2–3 μm, 2.20 min)	8 : 06 : 16 (HST, 555 nm, 3 min) 8 : 06 : 17 (Galileo SSI, 560 nm, 2.3 s)	$\gtrsim - 40$ s

As was mentioned in Ref. [4], a strong correlation exists between the values of effects observed (ejection size, radiation intensity, etc.) and sizes of fragments measured by analyzing their images (see Table 2). Exceptions are those fragments that resulted from the secondary fragmentation. As was noted above, these 'young' splinters probably had an excessive dust concentration inside the coma, so the size of their nuclei seemed larger than it actually was. For example, the A fragment impact caused a brighter ejection than that caused by impact of the secondary fragments Q1 and Q2, although according to photometric estimates their relative size was significantly larger. It is also important to point at a significant feature connected with the moment of appearance of the Pc1 in the light curves obtained on Earth, the moment of registration of the first outburst by the HST and the time that corresponds to the beginning of the sharp increase of the light curves taken by the Galileo. A comparison of these moments was done in Ref. [23] and is presented in Table 4. As follows from this table, for all but W fragments, the first appearances of signal were registered at ground-based telescopes and only then, with a time delay of a few seconds, at the instruments installed on the Galileo and HST.

Based on observations of the comet taken during its approaching to Jupiter, astronomers calculated time and sites of the fragments fall on to the planet surface [24]. In Table 5 the comparison of the calculations and observations is presented and parameters that we will use in further discussion are listed (in particular, the time interval between the impact and appearance of the impact site on the visible part of Jupiter is indicated). Since all impact sites lie close to the latitude 45°, and since during the fall on Jupiter the splinters flied almost parallel to the planetary rotation axis, the slanting angle at which the splinters entered the Jovian atmosphere was 45° with respect to the local vertical line. As seen from the table, for most fragments the time and site of impact were calculated accurately enough. The impact time

(in the present table) was the moment at which the HST detected the first outburst.

Spectrophotometric observations and a number of other work were also obtained with the ground-based telescopes and HST. These results are considered in detail in the next Section in the context of interpretation of the data obtained with the purpose of constructing a unified physical model of processes that accompanied the SL9 fragments impact.

3.3 The interpretation of the data obtained
Since the cometary fragments encounter with Jupiter a lot of papers have appeared that consider theoretical aspects of this event. Almost all they can be subdivided into two main groups. Those falling into the first group are devoted to modelling gas dynamic processes during SL9 fragments braking in the atmosphere [1, 25 – 29]. In most papers from this group, methods of direct numerical modelling were used, which allowed a sufficiently accurate description of the braking and destruction of cometary fragments. However, an adequate description of large-scale gas dynamic processes caused by a powerful energy output during fragments braking has met serious numerical difficulties (for example, it is impossible to provide sufficient spatial discretisation for calculations in a three-dimensional region with a linear size of several hundred km). For this reason, to describe large-scale effects, authors of some papers [29 – 34] used semi-quantitative analytical models, in which the results of numerical calculations of fragments braking were taken as the input data.

In the second group of theoretical works, different individual effects observed during the comet fragments fall were considered. Based on the results of papers from the first group, authors from the second group of publications have offered their own interpretation of the observational data. The analysis of the results obtained in papers from both groups enabled the authors to compare them with observations and, based on this comparison, to give preference for

Table 5

	Predicted impact data			Results of observations				
Fragments	dd : hh : mm : ss, UT	Latitude, degrees	Longitude, degrees	HST observations, latitude, degrees	HST observations, longitude, degrees	HST observations, accepted impact time, UT hh : mm : ss	Crossing the limb, min after the impact	Crossing the terminator, min after the impact
A	16 : 19 : 59 : 42	−43.15	178	−43.54 ± 1.0	186.3 ± 2.0	20 : 13 : 24 ± 3	19.4	37.6
B	17 : 02 : 54 : 15	−43.17	70	−42.79 ± 1.0	71.1 ± 2.0	02 : 56 : 09 ± 3	20.2	38.4
C	17 : 07 : 02 : 15	−43.38	218	−43.41 ± 1.0	225.0 ± 2.0	07 : 13 : 51 ± 3	18.1	36.3
D	17 : 11 : 47 : 02	−43.46	30	−43.29 ± 1.0	33,5 ± 2,0	11 : 52 : 50 ± 3	17.4	35.6
E	17 : 15 : 04 : 47	−43.48	149	−44.54 ± 1.0	153.5 ± 2.0	15 : 12 :11 ± 3	16.9	35.1
G	18 : 07 : 28 : 53	−43.60	23	−43.66 ± 1.0	26.8 ± 2.0	07 : 35 : 11 ± 3	15.6	33.8
H	18 : 19 : 26 : 03	−43.74	97	−43.66 ± 1.0	101.4 ± 2.0	19 : 33 : 21 ± 3	15.1	33.3
K	19 : 10 : 18 : 22	−43.80	275	−43.29 ± 1.0	282.6 ± 2.0	10 : 30 : 58 ± 3	13.7	31.9
L	19 : 22 : 09 : 08	−43.92	344	−42.79 ± 1.0	351.6 ± 2.0	22 : 21 : 44 ± 3	13.1	31.3
N	20 : 10 : 20 : 03	−44.30	66	−43.41 ± 1.0	73.1 ± 2.0	10 : 30 : 09 ± 3	13.4	31.6
Q2	2 : 19 : 47 : 19	−44.26	48	−44.67 ± 1.0	47.5 ± 2.0	19 : 46 : 31 ± 3	11.9	30.1
Q1	20 : 20 : 04 : 48	−44.05	58	−43.41 ± 1.0	66.3 ± 2.0	20 : 18 : 24 ± 3	11.2	29.4
R	21 : 05 : 28 : 24	−44.07	39	−44.50 ± 1.0	43.6 ± 2.0	05 : 36 : 06 ± 3	11.0	29.2
S	21 : 15 : 12 : 46	−44.16	31	−43.91 ± 1.0	34.0 ± 2.0	15 : 17 : 46 ± 3	10.3	28.5
W	22 : 08 : 00 : 52	−44.15	280	−44.29 ± 1.0	284.8 ± 2.0	08 : 08 : 46 ± 3	9.3	27.5
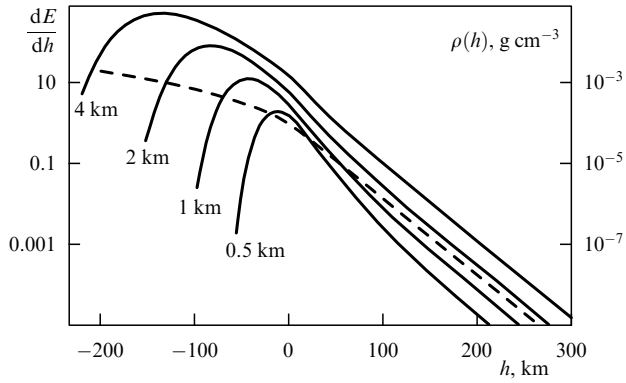
Figure 12. The thermal energy dE/dh (relative units) released per unit trajectory length as a function of the altitude h. The solid lines correspond to results of calculation of braking of fragments with different sizes according to the model [35], the dashed line represents the Jovian atmosphere density height profile. The angle of entry of fragments into the atmosphere is $45°$.

one of the initial models, as well as to make some conclusions on the possible chemical composition of the Jovian atmosphere and the SL9 nucleus.

Fig. 12 shows a typical dependence of the energy output along the trajectory on the altitude. The curves were obtained using a simple hydrodynamic model [35] that describes the body deformation assuming the constancy of its volume (without ablation) under the action of aerodynamic drag force. The difference between the results of this simple model and data of numerical modelling of braking and destruction of cometary fragments with different form, density and strength [27] turns out to be not very significant until the moment when strong evaporation and destruction of the fragment material begins. There is nothing specially surprising in that the simple model [35], which reduces to four ordinary differential equations, provides the acceptable accuracy of description. At an early stage of the fragment motion in atmosphere, when aerodynamic load does not affect noticeably its motion and does not lead to a significant deformation of the nucleus, the amount of thermal energy released per unit trajectory length is directly proportional to the atmospheric density which depends exponentially on the altitude. Therefore, at large altitudes $dE/dh = \text{const}$ $\rho(h) \propto \exp(-h/\Delta)$, which is clearly seen in Fig. 12. As the fragments move down, the mass of captured atmospheric gas increases rapidly, and when it becomes comparable to the fragment mass, the stage of substantial braking begins. This occurs at altitudes corresponding to the following density of the ambient gas:

$$\rho_s \sim \rho_i \, \frac{D_i \cos\theta}{3\Delta} \,, \tag{1}$$

where $\theta \simeq \pi/4$ is the slanting angle of the fragment with respect to the local vertical line, ρ_i is the fragment material density and D_i is its diameter. The ram pressure at these altitudes far exceeds the strength for the cometary material, so the fragment strength does not affect significantly the shape of dE/dh. The height-scale Δ in the Jovian atmosphere depends strongly on the altitude h above the level where the pressure of the ambient gas $p = 1$ bar and the corresponding density is $\rho = \rho_0 = 1.7 \times 10^{-4}$ g cm^{-3}: at altitudes where

$p \geqslant 1$ bar the density changes according to the law $\rho = \rho_0(1 - h/\Delta)^{2.27}$, $h \leqslant 0$, $\Delta \simeq 75$ km; for $p \leqslant 1$ bar, $\rho = \rho_0 \exp(-h/\Delta)$, $h \geqslant 0$, $\Delta \simeq 23$ km (see, e.g., Ref. [30])†.

Assuming the cometary fragment density $\rho_i \sim 1$ g cm^{-3}, which corresponds to the density of ice, the diameter $D_i \simeq 2$ km, we find that the fragment undergoes most braking at the ambient gas density $\rho_s \simeq 2 \times 10^{-3}$ g cm^{-3} and pressure $p_s \simeq 35$ bar. This corresponds to the altitude $h_s \simeq -140$ km in the Jovian atmosphere and agrees well with a maximum of dE/dh for a fragment of 2 km across (see Fig. 12). As is seen from the plot, by approaching the maximum, increase of dE/dh becomes more and more rapid (relative to the atmospheric density increase). This is due to the fact that increasing aerodynamic loads at the stage of substantial braking leads also to significant plastic deformations of the fragment, thereby significantly increasing its cross-section. For this reason, the ratio of dE/dh to the atmospheric density near the maximum of energy output turns out to be an order of magnitude larger than that at the early stage of braking. The difference of numerical modelling data from the results of the simple model [35] described above is that in this case the maximum of dE/dh proves to be somewhat shifted toward the region of higher altitudes (and densities, respectively). This is connected with the fact that at the late stage of braking the nucleus is completely destroyed and partially evaporated, which is not taken into account in the model [35]. This leads to a faster increase of the cometary nucleus cross-section. In addition, the Rayleigh–Taylor and Kelvin–Helmholtz instabilities start to develop on the liquid surface [36], which also increases the fragment cross-section and leads to even sharper growth of dE/dh curve.

Thermal energy released during the cometary fragment braking leads to a strong shock wave (SW) generation. As follows from Table 2, the mean fragment size is about $1 - 3$ km, which for the relative fall velocity $v_i \simeq 60$ km s^{-1} corresponds to the kinetic energy of the order of $10^{28} - 10^{30}$ erg. The pressure beyond the SW front caused by such an enormous energy release exceeds considerably the pressure of the ambient atmosphere. In other words, the SW intensity is so high that the ratio of densities after and before the wave passage is equal to a limiting value $(\gamma + 1)/(\gamma - 1)$, where γ is an effective adiabatic index of the atmospheric gas. Therefore to describe the initial stage of the SW expansion we may take a self-similar solution of the strong cylindrical explosion problem [37] using the fact noted above that at the early stage of the fragment braking the ratio $\rho^{-1}(dE/dh)$, which enters the only dimensionless parameter of the problem, $r(\rho/t^2)^{1/4}(dE/dh)^{-1/4}$, is constant ($r$ is the radius of the cylindrical SW, t is the time). That the energy release along the line of motion of the fragment occurs not simultaneously, cannot affect significantly the results of semi-qualitative considerations. Indeed, to the moment of time $\tau_s = \Delta/v_i \leqslant 0.5$ s, which takes the fragment to fly the distance Δ (the time is counted beginning from the moment of passing a given point by the fragment), the front radius of the cylindrical SW is equal to $r_D = \Delta(D_i/64\Delta)^{1/4}$ according to Ref. [37]. Since $D_i \simeq 1 \div 4$ km and $\Delta \geqslant 25$ km, the value of r_D

† According to the preliminary data [2] obtained during the Galileo probe penetration into the dense atmospheric layers of the planet, the height-scale Δ is larger than that used normally in models, i.e. the density decreases slower with altitude than was expected. This, while not changing our subsequent considerations, may change specific estimates of the depth of fragments penetration and their sizes.

turns out to be appreciably smaller than Δ but larger than D_i. In addition, the duration of cylindrical SW existence $(\mathrm{d}E/\,\mathrm{d}h)^{1/2}\rho^{-1/2}/4c_s^2$ exceeds the time τ_s (c_s is the sound speed in the Jovian atmosphere, $c_s \simeq 1$ km/s) by more than an order of magnitude. For these reasons, the use of self-similar solution of the problem of a strong cylindrical explosion on a time-scale $t \geqslant \tau_s$ is well justified for our estimates. It is easy to verify that our initial assumption that the SW is strong at early stages of expansion is correct. For this, it is sufficient to compare the atmospheric pressure p with the mean pressure p_D after the SW front, which is equal, by an order of magnitude, to the energy released per unit length $\mathrm{d}E/\,\mathrm{d}h$, divided by the area S_D of a circle with radius r_D. The area is $S_D \simeq \pi D_i^2 (\Delta/4D_i)^{3/2}/4$, and the corresponding pressure is

$$p_D \sim \frac{(\gamma-1)}{2S_D}\,\frac{\mathrm{d}E}{\mathrm{d}h} \sim (10^2 \div 10^4)\,p. \qquad (2)$$

At the stage of substantial braking, when $\mathrm{d}E/\,\mathrm{d}h$ begins increasing much faster than $\rho(h)$, using the cylindrical explosion approximation becomes incorrect. However, as is seen from Fig. 12, the spatial scale of the intensive energy release does not exceed Δ, and the amount of energy liberated is of the order of the initial kinetic energy of the fragment E_0. Therefore, to describe the initial stage of motion of the SW resulted from energy release in the given region, we use a solution of the strong point explosion problem [33, 37]. Using the total momentum and energy conservation law for the whole system (the moving fragment material plus the captured atmospheric gas), it is easy to obtain the temporal dependence of the thermal energy released at the stage of substantial braking [34]:

$$E(t) \simeq \mathrm{e}^{-1}E_0 + (1 - \mathrm{e}^{-1})\,E_0\,\frac{t/\tau_s}{1 + t/\tau_s}. \qquad (3)$$

The time t is counted from the moment when the fragment reaches atmospheric layers with a density of order ρ_s and its noticeable braking begins. Since this occurs at altitudes lower than 1-bar level, where $\Delta \simeq 70$ km, then $\tau_s \simeq 1$ s. Thus, in a time period t_0 of order of several τ_s an energy close to E_0 is released, so one should substitute $E = E_0$, $\rho = \rho_s$ and $t \geqslant t_0$ into the self-similar parameter, which is $r\,(\rho/t^2)^{1/5}E^{-1/5}$ in the case of a point explosion. Using the point explosion model to describe the SW evolution on time scales $t \geqslant t_0$ is well justified, as the diameter of the spherical front of the wave (at the fragment energy $E_0 \sim 10^{30}$ erg) will be of the order of 100 km to this moment according to Ref. [37], i.e. larger than Δ and much larger than D_i.

3.3.1 Interpretation of data obtained with the Galileo space-craft.
In order to understand what was the source of emission registered at the Galileo spacecraft, as well as to explain the form of light curves obtained, we consider physical processes occurring beyond the SW front as the wave weakens. Since the temperature beyond the front of a high intensity SW, T_f, is proportional to the square the wave velocity D, which, in turn, depends on the front radius r_f as $\propto r_f^{-1}$ in the case of cylindrical symmetry and as $\propto r_f^{-3/2}$ in the case of spherical symmetry, T_f drops rapidly enough down to a few thousand degrees. At the same time, the temperature increases very rapidly toward the explosion centre: $T \simeq (r_f/r)^{(2\gamma+1)/(\gamma-1)}\,T_f$. Thus, beyond the SW front a region of hot ionised atmospheric gas exists, and if gas density (about 90% of the atmosphere consists of hydrogen) is sufficiently high, this region is optically thick. Using the Unzold–Kramers formula

[38] for the total absorption coefficient in ionised gas, we are able to estimate an upper boundary of the atmosphere beyond which the shock-wave-heated gas cannot be optically thick: this altitude is about 200 km above the 1-bar level. The optically thick gas beyond the SW front radiates with a transparency temperature T_{opt} [38], which is determined from the condition that the inverse absorption coefficient corresponding to a given temperature coincides on the order of magnitude with a spatial scale of the temperature variation. T_{opt} is directly proportional to the ionisation potential I and depends logarithmically on the gas density; in the case of hydrogen plasma, $T_{\mathrm{opt}} \simeq 15000$ K. The gas layer with the temperature T_{opt} moving behind the SW front cools down primarily due to radiation, which leads, as the SW relaxes, to the formation of a temperature jump and a radiation cooling wave [38] moving toward the explosion centre with the velocity

$$u \simeq 2\,\frac{\gamma-1}{\gamma}\,\widetilde{\delta T}_{\mathrm{opt}}^{-1}\,\frac{\sigma T_{\mathrm{opt}}^4}{p} \qquad (4)$$

with respect to the expanding gas, where $\widetilde{\delta T}_{\mathrm{opt}} \simeq kT_{\mathrm{opt}}/I$ [38]. As follows from (4), the cooling wave velocity u depends exponentially on altitude. At the early stage of braking, which for fragments more than one kilometre across continues up to the upper boundary of cloud cover ($p \simeq 0.3$ bar), the velocity u is of the order of 10 km/s. The cylindrical SW velocity becomes comparable with u about one second after the SW appearance, the cooling wave radius r_{opt} attains then a maximum value and is nearly equal to the SW radius $r_f \simeq 30 - 40$ km. Then the gas bulk velocity behind the SW front becomes smaller than u, so the cooling wave radius (and, hence, the area of emitting surface) begins decreasing. Therefore, the time during which an effective emission occurs from a region heated up higher than the cylindrical SW clouds, may be estimated as not exceeding $r_f/u \simeq 5 - 6$ s. Here the maximum emission region follow the fragment at some distance from it. Obviously, this distance is determined by the time during which the radiative cooling wave radius r_{opt} reaches a maximum value. Since the duration of this emission proves to be relatively short, dense atmospheric gas heated up during the early braking stage is sometimes called by meteor track.

The emission of gas heated up below the cloud layer is screened during a few second until the impact-induced heating evaporates aerosols that form the cloud cover and the expanding SW produces a sufficiently big hole in the cover. Therefore this emission can be time-delayed by $1 - 2$ s from the meteor track radiation. Simultaneously with the hole expansion, a strong braking of the fragment begins at altitudes corresponding to the atmospheric pressure of $p = p_s \simeq 10$ bar and a SW emerges for which we use the point explosion model. The radiation cooling process in this case will not differ qualitatively form the cylindrical explosion example considered above, however the cooling wave velocity at altitudes corresponding to a maximum energy release level will be an order of magnitude less and the duration of efficient emission from this region will be about $40 - 50$ s. This region bounded by the cooling wave front r_{opt} is often referred to as a fireball†.

---

† The term 'fireball' is used to describe the region of a hot emitting gas produced by an atmospheric nuclear explosion. Radiation and gasdynamic processes occurring in the region of most energy release during a comet impact are similar to those in the fireball of nuclear explosion.

It is not difficult to obtain the equation of motion for the fireball surface [32]. In the case of a point explosion, the equation and its solution have the form:

$$\frac{dr_{opt}}{dt} = \frac{2}{5} \frac{2}{\gamma + 1} \frac{r_{opt}}{t} - u_s, \tag{5}$$

$$r_{opt}(\tau) = r_0[(1 + \beta)\tau^{0.8/(\gamma+1)} - \beta\tau], \tag{6}$$

where $\beta = 5(\gamma + 1)u_s t_0/(5\gamma + 1) r_0$, $\tau = t/t_0$, r_0 is the radius of a layer with temperature T_{opt} at the moment t_0, i.e. the initial radius of the cooling wave; for a fragment with energy $E_0 \simeq 10^{30}$ erg $r_0 \simeq 40$ km. Radiation will escape the cloud cover through a hole whose diameter is equal to the diameter d of the cylindrical SW, which already relatively weakens to this moment of time. The value of d is a few $D_i (\Delta/4D_i)^{3/4}$ and the intensity of emission I_λ is proportional to $\Omega \simeq d^2/h_s^2$, where h_s is the altitude of explosion relative to the 1-bar level. Thus, the radiation intensity, which may be detected at the Galileo, is determined by the following equation:

$$I_\lambda(t) \simeq \frac{8\pi ck T_{opt}}{\lambda^4} \frac{r_{opt}^2(t)}{R_{JG}^2} \Omega, \tag{7}$$

where $R_{JG} \simeq 1.5$ AU is a distance between Jupiter and the Galileo. Fig. 6 demonstrates the dependence $I_\lambda(t)$ given by (7). This dependence corresponding to the diameter $D_i \simeq 3$ km or energy $E_0 \simeq 3 \times 10^{29}$ erg provides a good approximation to the light curve obtained during the L fragment fall. Using (1) and (4), it is straightforward to show that the fireball emission duration is proportional to $D_i^{1.4}$ and the maximum intensity $I_\lambda^{max} \propto D_i^{1.3}$. The sizes of the G and H fragments estimated using the latter relation were found to be 2.6 km and 2.2 km, respectively. It is impossible to estimate the size of the Q1 fragments, because the corresponding light curve consists of a sequence of relatively weak peaks apparently caused by the fragment splitting into several small-size fragments during fall to Jupiter. As we mentioned at the end of Section 3.2, the splinters emerging as a result of the secondary fragmentation caused less spectacular observational appearances than one might expect based on estimates listed in Table 2, since actual sizes of these fragments were smaller than the predicted ones. That the L fragment, according to our calculations, turned out to be somewhat larger in size than the fragment G may be explained by namely this fact. The possible absorption of radiation at the wavelength $\lambda \simeq 945$ nm in the Jovian atmosphere, as well as multiple diffuse scattering by aerosol particles inside the hole formed, may lead to the actual fragment sizes being larger than those obtained by using (7). Based on estimates of D_i for the fragments G, H, and L, we can determine the parent body size. It is not less than $4 - 5$ km across, which confirms indirectly the 'ice conglomerate' model [7] for the SL9 comet nucleus. An interesting feature of equation (7) is that the intensity $I_\lambda(t)$ proves to be dependent on the fragment size only, but not on its density ρ_i, as according to (1) the density ρ_s at the altitude of explosion is proportional to ρ_i. Since the real density of a fragment may differ significantly from 1 g cm^{-3} (for example, in Ref. [7] the density of fragments is estimated to be $\rho_0 \simeq 0.2$ g cm^{-3}), it is hard enough to find the fragment energy.

Thus, the model considered describes well enough the PPR light curves. The SSI light curves obtained at the wavelengths $\lambda = 0.89$ μm (see Fig. 8) and $\lambda = 0.56$ μm are

exceptions. The first maximum in the light curves for the K and N fragments is apparently connected to the meteor track emission. However, a time interval between the first maximum and the second longer outburst can not be explained by the hole expansion in the cloud cover, because the corresponding time delay is shorter than $1 - 2$ s. Most probably, this time interval is caused by the absorption of fireball radiation by methane molecules, which are present in the atmosphere with an abundance of a few tenth percent, and the vertical optical depth in the atmosphere caused by absorption in strong bands of CH$_4$ at the wavelengths $\lambda = 0.89$ μm and 0.56 μm becomes equal to unity at the pressure level $\leqslant 0.3$ bar [39], i.e. practically at the upper cloud boundary. Methane molecules start dissociating efficiently at temperatures $T_{diss} \simeq 4000 - 5000$ K, so the region within the cylindrical SW front can be subdivided into three conditional regions: (a) $0 \leqslant r \leqslant r_{opt}$, the region of optically thick meteor track; (b) $r_{opt} \leqslant r \leqslant r_{diss}$, the region of transparency at given wavelengths (radius r_{diss} corresponds to the temperature T_{diss}); (c) $r_{diss} \leqslant r \leqslant r_f$, the region beyond the SW front with a temperature inside not exceeding T_{diss}. For radiation at wavelengths corresponding to CH$_4$ absorption bands, only the (b) region is transparent; for radiation at other wavelengths at which observations were performed, the (b) and (c) regions are transparent. Temperature increases from the SW front towards the explosion centre according to a power law, so when the SW relaxes and $T_f \ll T_{opt}$ but the cooling wave radius r_{opt} still does not start decreasing, we obtain that $r_f - r_{opt} \gg r_{diss} - r_{opt}$, i.e. the (c) region area is much larger than that of the (b) region. For this reason, the fireball emission at wavelengths $\lambda = 0.89$ μm and 0.56 μm goes outside only after the cooling wave has made the meteor track 'transparent' along the total height from the transparency boundary of the atmosphere in the methane bands up to some conditional boundary within the fireball, where the pressure is p_{upper}. The emission absorption coefficient is proportional to pressure, so the condition that the fireball emission begins escaping outside through the meteor track transparent up to the level p_{upper} is equivalent to the condition that the ratio of the pressure inside the fireball and the pressure p_{upper} is of order of e. The time interval t_{tr} during which the meteor track becomes transparent is $t_{tr} \propto u^{-1} \propto p_{upper}$. Therefore, the total duration of the fireball emission and the time t_{tr} must be also of the same order, which is actually the case. According the mechanism proposed, small-size fragments may cause only short radiation outbursts from the meteor track located above the boundary of atmospheric transparency in methane bands. As pointed above, the duration of the fireball emission $\propto D_i^{1.4}$, so for small fragments (such as N) it must be about four times shorter than for the K fragment, i.e. of the order of 10 s. The duration of the meteor outburst then will not depend on the fragment size, because this duration is determined only by the time of the fragment motion from the altitude of 200 km down to the boundary of transparency in methane bands and by the duration of the meteor track glowing at this level.

In Section 3.1 a short note was made that a number of light curves obtained with the NIMS device in the IR band have one significant difference from all other light curves. This difference is that the intensity (Fig. 7b) increases much smoother at the light curve beginning (during approximately $10 - 15$ s). No sufficiently reliable explanation has been suggested so far in the literature for such a behaviour. The smooth increasing of the light curve most likely appears to be

connected to a strong absorption of radiation in the atmosphere during the first seconds after the explosion. Such an explanation is inspired by the fact that the feature considered was seen only in the light curves obtained at the wavelengths that corresponded to strong absorption bands of CH_4, NH_3, H_2, and other materials, which are present in the Jovian atmosphere. So shock-wave processes in the atmosphere, which are accompanied by non-equilibrium chemical reactions in the heated gas, may well be a reason for the time delay and the smooth increase discovered at the emission wavelengths pointed above.

In a number of papers an assumption has been made that the part of the meteor track that lies above the cloud layer ($h \geqslant 30$ km, $p \geqslant 0.3$ bar) is the source of emission detected by the Galileo. However, as shown above, the duration of outburst of the optically thick meteor track located above the cloud level should not exceed several seconds, which contradicts observational data. The transparent part of the meteor track located above the level $h \simeq 200$ km ($p \sim 10^{-4}$ bar) also cannot be the source of the emission observed, since in this case the emission is substantially non-equilibrium and its intensity (in the absence of pumping) decreases exponentially on a characteristic time scale determined as min $\{v^{-1}, A_j^{-1}\}$, where A_j^{-1} is the radiative lifetime of emitting molecule and v is the collision frequency between molecules inside the meteor track. It is easy to understand that the duration of such an equilibrium shining does not correspond to the observational data. Finally, the emitting energy is proportional to the amount of heat released along the comet line of fall (both in the case of optically thick and optically thin gas), which, in turn, increases exponentially as altitude decreases. Therefore in any case the source of the main radiation is the optically thick fireball region.

According to preliminary estimates, the fall of a cometary fragment on Jupiter could be accompanied by an increase in brightness of the planet's satellites. Such an optical echo, when the planetary satellites serve as a mirror reflecting the explosion outburst light, was discussed in some papers [1, 29] in which the emission power at a level of 10^{25} erg s^{-1} during impacts of sufficiently large fragment was predicted. Such an outburst could lead to the increase in brightness of the closest to Jupiter satellites (Io and Europe) of order of one percent. These forecasts provided observers with a certain optimism, so many astronomers tried to discover the optical echo. However, the emission intensity really detected by the Galileo spacecraft during large fragment impacts did not exceed a level of 10^{22} erg s^{-1} (that the Galileo was at these moments at a low height above the Jovian horizon does not change the subsequent estimates), so the brightness increase of satellites, if it were real, would be of order of several hundredth of percent, which is far below the precision of measurements. At present, there are no firm evidences indicating that during the SL9 impact the optical echo was discovered. In our opinion, they will hardly appear in future. Rapid brightness variability of some Jovian satellites observed during the impacts is likely connected to the fall of small-size (a few meter across) fragments of SL9, and has no relation with the optical echo caused by the large fragment impacts.

3.3.2 The interpretation of the data obtained on Earth and by near-Earth spacecrafts. Here we discuss the forms of light curves obtained on Earth and try to answer the question as to what the source of emission was to which the first two short outbursts (Pc1 and Pc2) and the main maximum in the

obtained light curves (see Fig. 11) correspond [21, 22]. For some fragments, the moment of appearance of Pc1 and its duration coincide relatively well with the outbursts of radiation registered at the Galileo [17 – 19]. This provides grounds to assume that in the case of impact of these fragments, the precursor Pc1 is caused by the fireball emission. Since the explosion itself occurred under the cloud layer, only a small part of the fireball radiation that escapes through the explosion-destroyed cloud cover region and scatters by the atmosphere may be observed on Earth. This is the reason for the low intensity of the Pc1 outburst. However, for some impacts listed in Table 4, the Pc1 precursor observed on Earth earlier than at the Galileo and HST, with a minimum time delay being of order 20 – 30 s. In this case, the reason for the delay may be the fact that the emission registered in ground-based observations was that of the upper atmosphere heated up by the dust coma, which surrounds each cometary fragment. The corresponding time delay τ can be evaluated by dividing the characteristic size of the coma (about 1 – 3 thousand km) by the fragment velocity ($v_i \simeq 60$ km s^{-1}), which yields $\tau = 30$ s. The Pc1 outburst duration in this case should be about two time as long as τ, i.e. of order one minute. The observational equipment onboard the Galileo and HST did not discover this emission since the outburst intensities were far below the sensitivity threshold of detectors [20]. Therefore, different origin of the Pc1 outburst for different fragments is most likely: in some cases, this is the fireball radiation after the fragment explosion, in other cases, the radiation of the upper atmosphere heated by the coma prior to the explosion.

The assumption that the Pc1 outburst (as well as the outbursts of radiation discovered at the Galileo) are caused by a thermal emission from the meteor track directly seen from Earth [40] can not explain observational data. Indeed, during the R fragment fall, the light curve of which is considered by us as an example (see Fig. 11), the part of meteor track directly seen from Earth is located at altitudes of 500 km above the 1-bar level, which is caused by a strong absorption by atmospheric methane at the given wavelengths [21]. The energy released by the fragment during braking at these altitudes can not provide the observed radiation fluxes (the energy released is $10^{-12}E_0$). Even for a fragment with an energy of 10^{30} erg ($D_i \simeq 4$ km), the heat released at these altitudes is by three orders of magnitude less than the total energy emitted during the Pc1 outburst. As follows from Table 5, the R fragment fell relatively close to the limb, so the Pc1 origin in other light curves cannot be explained by the meteor track all the more. However, the energy released during the coma braking is sufficient to explain the Pc1 outburst. According to the HST data, the coma of SL9 fragments consisted primarily of dust particles with a characteristic size of $0.1 - 10$ μm. The fragment entry into the Jovian atmosphere was accompanied by the separation of particles by sizes: it is easy to show that tiny particles less than 0.1 μm across are captured by the magnetic field, whereas the dust particles with a size larger than 1 μm pass through the magnetosphere practically without obstacle and perish in the Jovian atmosphere. At the altitudes of 500 km, dust particles with a characteristic size of 0.3 μm brake down. The dust component mass for large fragments of SL9 is estimated as 10^{10} g. Since the dust particles spend most of their kinetic energy at the altitudes that are of interest here ($h \geqslant 500$ km), the braking-induced energy release is $(10^{-6} \div 10^{-7})E_0$. This energy is sufficient to provide the emission flux observed in

Pc1 outburst. In order to explain the origin of the second and third outbursts we consider the part of the SW that propagates upwards in the direction of decreasing atmospheric density, which formed at the stage of strong atmospheric braking of the fragment. Once a distance passed by the SW matches with the height-scale Δ, inhomogeneity of the atmosphere begins to affect the propagation velocity D. First the SW velocity decreases with distance from the site of explosion as $D \propto R^{-3/2} \exp(R/2\Delta)$ [41] and attains a minimum D_{min} at $R \simeq 3\Delta$. As was shown in Ref. [30] (for an explosion at an altitude of $h_s \simeq -100$ km, the pressure $p_s \simeq 10$ bar, and energy $E_0 \simeq 10^{29}$ erg), beginning from a level of ~ 1 bar where the velocity $D_{min} \simeq 5-6$ km s^{-1}, the SW starts to accelerate. At this stage $D \simeq D_{min} \exp[(R - 3\Delta)/\alpha\Delta]$ [42], where α depends on the isoentropic index γ (for example, $\alpha \simeq 4.9$ for $\gamma = 5/3$ and $\alpha \simeq 6.5$ for $\gamma = 1.2$). The temperature of the shock-compressed gas T is proportional to D^2 and $T_{min} = T_{min}(D_{min}, \gamma) \simeq 2000$ K. Notice that the shock-compressed gas starts expanding and cooling adiabatically immediately after the SW passage. The characteristic cooling time after the shock compression increases with time from several seconds (just after the SW passage) to a few tens seconds at a late stage of the cooling [42]. As a result, at the late stage (about 10 s after the SW passage) the minimum temperature of the shock-heated gas drops down to $T \simeq 1000$ K.

When the temperature behind the SW front reaches several thousand degrees, a large number of chemical compounds, which are usually absent in the Jovian atmosphere, begin forming. In addition to hydrogen, in the unperturbed atmosphere a few percent of helium, a few tenth percent of CH_4, as well as NH_3, NH_4SH and H_2O are present, which form three consecutive layers of the cloud cover. In Ref. [43] the results of numerical calculations of the equilibrium chemical composition of gas heated up to temperatures of the order of several thousand degrees are presented. A maximum temperature in all calculations did not exceed $T_{diss} \simeq 5000$ K, because at higher temperatures an intensive dissociation of nearly all chemical compounds, the formation of which is possible from the original atomic composition, begins. At lower temperatures, in the hot gas such compounds as CO, NH, CH, HCN, CN, N_2, CS, CH_4, etc. start forming. Here the carbon monoxide is especially notable, whose mole composition is at a level of 10^{-3} over all temperature range. The most critical parameter that determines the gas composition is the mole ratio of oxygen and carbon [O]/[C] since most molecules forming during this process contain carbon. However, an important note should be made relative to the results of equilibrium thermodynamic calculations at sufficiently low temperatures. As the gas expands and cools down, the chemical reaction rates decrease and the characteristic chemical relaxation time increases. When the relaxation time becomes comparable with the characteristic time of temperature change, the quench effect occurs [38] and the relative molecule concentrations remain practically unchanged during the subsequent cooling, staying at a level that corresponds approximately to an equilibrium concentration at the quench temperature T_*. No sufficient data on T_* for the reactions under consideration are available in the literature. However, in most cases the quench occurs at temperatures near 1500 K. For this reason the concentration of many molecules at the temperature $T \simeq 1000$ K is much higher than that obtained using the equilibrium thermochemical model. Our interest to chemical compositions appearing in the shock-heated gas is caused by some of these molecules contributing effectively to the optical thickness. Therefore in the case of a sufficiently high density the shock-compressed gas can radiate as a black body with a maximum spectral intensity at the frequency $\omega_m \simeq 2.8\, kT/\hbar$; the corresponding wavelength is $\lambda_m \simeq 5.1 \times 10^3/T$ μm.

As the SW accelerates, the temperature of the shock-compressed gas increases, $T \propto D^2$, which shifts the radiation spectral intensity maximum to the shorter wavelengths. Therefore, at the moment of appearance of the optically thick gas its temperature is $T \simeq 1000$ K and $\lambda_m \simeq 5$ μm. Then, as the SW accelerates further, during the time period $t_{diss} \simeq \alpha\Delta/2D_{min} \simeq 15$ s the temperature reaches T_{diss}, and λ_m decreases to about 1 mm. After that the temperature behind the SW front exceeds T_{diss} and all molecules that are capable of absorbing in the visible and IR bands dissociate thus making the gas optically transparent. As a result, the propagation of a strong SW upwards in the inhomogeneous atmosphere leads to the formation of a layer that moves upwards and radiates as a black body with the initial temperature changing from $T \simeq 1000$ K to T_{diss}.

Let us consider the second precursor Pc2 in Fig. 11. As was noted in Ref. [21], the spectral intensity for the Pc2 decreases more smoothly at shorter wavelengths, but at the beginning the longer wavelength, the higher intensity is. According to our model, the SW propagation leads to the generation of the optically thick gas layer. At the moment of its appearance, the gas temperature in the layer is sufficiently low and its radiation at wavelengths $\lambda = 2.3$ μm, 3.2 μm, 4.5 μm is determined by the Wien law ($T \simeq 1000$ K, $\lambda_m \simeq 5$ μm), so the radiation intensity increases more smoothly at lower wavelengths. As the temperature increases behind the SW front, the spectral intensities at $\lambda = 4.5$ μm, 3.2 μm, and 2.3 μm go over successively into the Rayleigh–Jeans region ($\hbar\omega \leqslant kT$). This transition occurs by the time $t \simeq t_{diss}$ after the optically dense layer has appeared with the temperature $T \simeq T_{diss}$ and $\lambda_m \simeq 1$ μm. The subsequent rapid expansion of the shock-compressed gas causes the decreasing of the temperature and size of the optically dense region. Therefore during this period of time the spectral intensity of the gas radiation, which obeys the Rayleigh–Jeans law, decreases more smoothly at lower wavelengths. As the temperature decreases further, the inverse transition occurs back into the Wien region (first $\lambda = 2.3$ μm, then $\lambda = 3.2$ μm, and $\lambda = 4.5$ μm) and after that the longer wavelength, the higher the radiation intensity at these wavelengths is. Thus the complete qualitative agreement takes place between the model considerations and the IR observations of the second precursor. It is important to note that according to the results of the model suggested, the second precursor Pc2 can be absent or less pronounced in the case of the large cometary fragments fall, as in this case the minimum temperature behind the SW front may exceed $T_{diss} \simeq 4000 - 5000$ K, so the shock-compressed gas is optically transparent from the very beginning. This conclusion is also well consistent with observational data as the Pc2 was observed only during some fragment encounters.

Now we turn to a detailed discussion of the third peak — the principal maximum in Fig. 11. In Fig. 13 we present the A, E, G, and W fragment light curves. By comparing series of images in Fig. 9 with the light curves presented, it can easily be seen that the processes of expanding and decreasing of the glowing ejecta correlate well with the periods of the intensity increasing and decreasing. In addition to these fragments, the
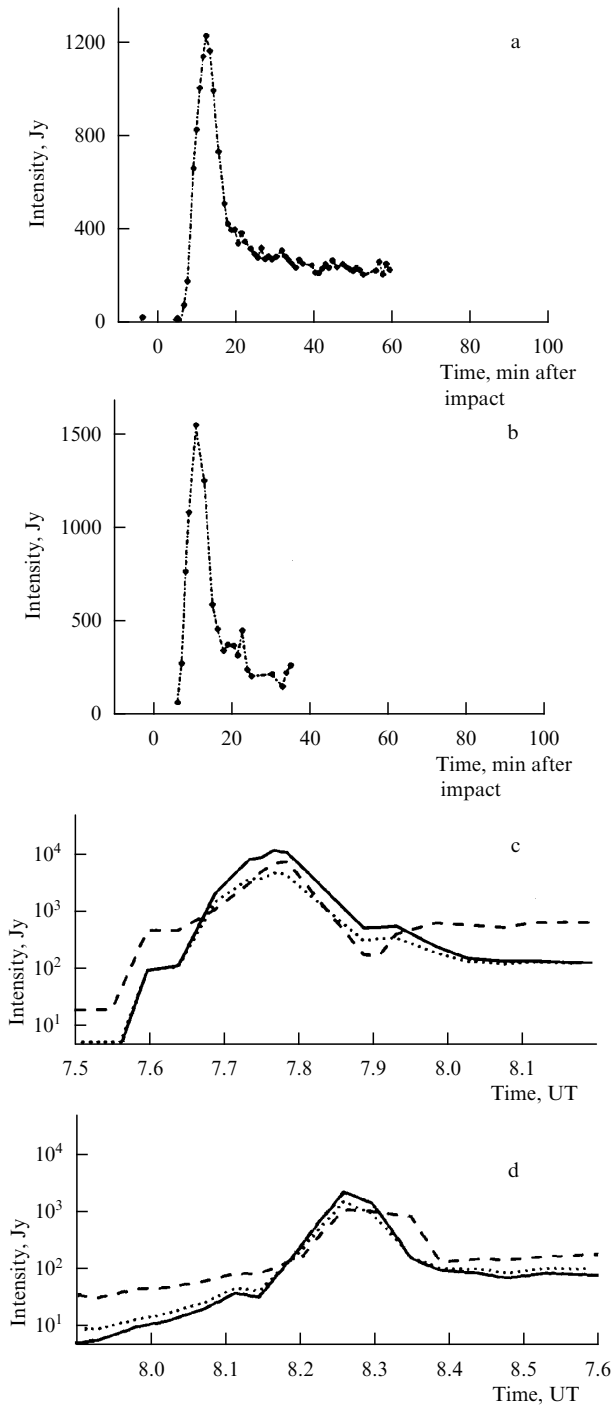
Figure 13. Light curves of Jupiter according to the ground-based IR observations of the A, E [46], G, W [53] fragment impacts. Matching these light curves with images of ejecta caused by the same fragments (Fig. 9) shows that the maximum in the light curve corresponds in time to the maximum ejection size.

equally good correspondence is found for other fragments, for which the ejections were detected during the encounter and light curve were simultaneously obtained. We have in our disposal such data for the K [44] and L [45] fragments. In addition, according to the spectral observations, the radiation temperature of the principal maximum decreased monotonically with the radiation intensity growth, by varying from about 1000 K at the moment of the main maximum

appearance to a few degrees K near the intensity maximum [46]. The radiation spectrum during the intensity growth is almost continuous and is well described by a Planck distribution function in the frequency range considered. All this evidences that the reason for the main maximum appearance on the light curves is the radiation of the hot expanding gas ejected into the upper atmosphere.

Let us consider the processes occurring at a late cooling stage of the gas ejected into the upper atmosphere. Until the temperature of expanding gas exceeds $T_{\rm diss}$ (the corresponding SW velocity $D \geqslant 12$ km s^{-1}), all complex chemical compositions are dissociated and the gas is optically transparent. At this stage, the gas moves upwards almost inertially and in about a minute after the SW passage it reaches altitudes, beginning from which it is directly seen from Earth. The maximum altitude $H_{\rm max}$ the ejected gas reaches is determined by the initial velocity acquired at the moment of the SW passage and is approximately $H_{\rm max} \simeq D^2/2g \simeq$ 3000 km. The gas expansion is described by a self-similar solution [42].

According to Ref. [42], the expansion is initially quasi-one-dimensional and the gas concentration changes according to the law $n \propto (t/t_l)^{-1}$, where t_l is the characteristic expansion time at the late cooling stage (this time depends on the explosion altitude: for the layer considered $t_l \simeq 20-30$ s [30]). The space inhomogeneity scale for the layer Δ_L increases as $\Delta_L \simeq \Delta(t/t_l)$. The temperature decrease is determined by the adiabatic expansion only, which becomes three-dimensional with time: $n \propto t^{-3}$, $T \propto n^{\gamma-1} \propto t^{-3(\gamma-1)}$.

When the temperature of the optically transparent gas decreases to $2000 \div 3000$ K, the molecular compounds that are capable of absorbing effectively the IR radiation begin to form, which results in a rapid increase in the gas optical thickness. The cooling from temperatures $5000 \div 7000$ K to $2000 \div 3000$ K occurs during a period of time of order $(5-10)t_l \simeq 200-300$ s.

Therefore, the SW leads to the ejection of the hot atmospheric gas into altitudes of some thousand km. As a result of the adiabatic expansion, the gas which is directly seen from Earth becomes optically dense about $4-5$ min after the fragment impact and has a temperature $T \simeq 2000-3000$ K by this time. The absorption coefficient of the hot gas κ_ω may be estimated using the expression [38]:

$$\kappa_\omega \simeq \frac{2\pi^2 e^2}{mc} \frac{\hbar}{kT} \sum_i f_i N_i \exp\left(-\frac{E_i - \hbar\omega}{kT}\right), \qquad (8)$$

where e, m are the electron charge and mass, f_i is the oscillator force, N_i is the concentration of molecules that absorb IR radiation, $\hbar\omega$ is the photon energy, and E_i is the energy of the excited level. At temperatures of some thousand K the absorption in the gas is due to electron transitions to low vibration levels of the upper electron state. As the temperature decreases, the absorption due to transitions to the upper vibration levels prevails, and the absorption coefficient is also dependent exponentially on temperature. Using (8) we may estimate the optical depth $\tau_{\rm opt}$ of the heated gas. Assuming $N_i \geqslant 10^{16}$ cm^{-3}, $E_i \simeq 1$ eV, $T_0 \simeq 2000$ K, $f_i \simeq 10^{-4}$, we obtain $\tau_{\rm opt} \simeq \kappa_\omega \Delta \simeq 10^3 - 10^4 \gg 1$. Therefore, the initial thickness L_0 of the optically dense layer $L_0 \simeq \Delta \ln \tau_{\rm opt} \simeq 10\Delta \sim 250$ km, and the initial transverse size of the layer is $d_0 \simeq 2\pi\Delta \simeq 150$ km [41].

Microscopic aerosol particles that form during the adiabatic gas expansion may also influence the optical depth

of the hot gas [39, 47]. Fig. 14 shows the results of calculations of condensation of some species which are present in the expanding gas [39]. These calculations were performed on the basis of a simple numerical model [48]; similar calculations were also performed in Ref. [47] based on the model [49]. The circles at two different adiabates shown by dotted lines correspond to the beginning of condensation of the corresponding materials. The solid lines correspond to levels of constant particle size R (μm). Therefore, in a temperature range from a few hundred to 1000 degrees the condensation of such species as SiO_2, H_2O and CS_2 occurs. The condensation of other materials, which can be present in the heated gas according to calculations of the chemical composition, begins at significantly lower temperatures than were found during the spectral observations. By knowing the concentration of given compounds in gas and the mean size of aerosol particles, it is not difficult to estimate the optical depth of the heated gas layer using Rayleigh ($\lambda \gg R$) or Mie ($\lambda \leqslant R$) formulae for the radiation scattering cross-sections. The optical depth caused by the condensing aerosol proves to be a few order of magnitude less than in the case of the molecular absorption discussed above, so this mechanism seems less likely to operate.

To estimate the radiation flux from the surface of the expanding gas, we need to determine how do the thickness and cross-size of the optically dense region change. The thickness L of the optically dense layer is obtained from the transparency condition: $\kappa_\omega \Delta_L \simeq 1$. The absorption coefficient may be estimated as

$$\kappa_\omega \propto n(z) T^{-1} \exp\left(-\frac{E_{\mathrm{eff}} - \hbar\omega}{kT}\right),$$

where E_{eff} is some effective excitation energy of the oscillatory transition, z is the coordinate (relative to the moving gas mass centre), so $n \propto \exp(-z/\Delta_L)$. Substituting $\Delta_L(t)$ and $T(t)$ into the transparency condition yields the equation for dependence of the optical thickness L on time
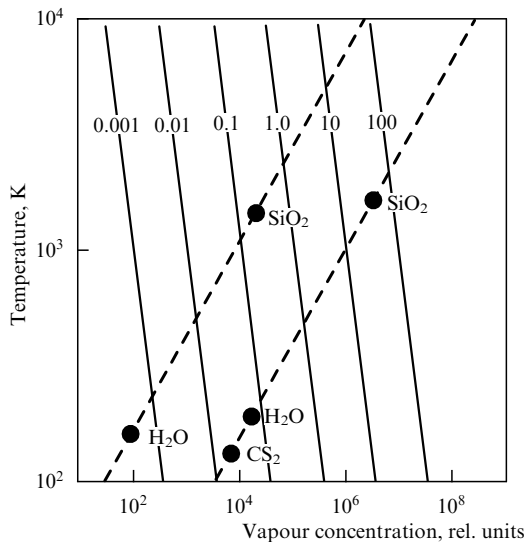
Figure 14. Aerosols that can be formed in a hot, adiabatically expanding gas of the ejection. The mean size of particles of the most probable aerosols and their formation temperature are indicated [39].

$$L(\tilde{t}) \simeq L_0\tilde{t}\left(1 - \frac{\Delta}{L_0}\left[(5-3\gamma)\ln\tilde{t} + \frac{E_{\mathrm{eff}} - \hbar\omega}{kT_0}\left(\tilde{t}^{3(\gamma-1)} - 1\right)\right]\right),$$

$$(9)$$

where $\tilde{t} = t/t_l$, $\tilde{t} \geqslant 1$. The radiation intensity of the expanding gas ejected into the upper atmosphere (at the limit $\hbar\omega \leqslant kT$) is given by the following expression:

$$I_\omega(\tilde{t}) \propto \tilde{t}^{4-3\gamma} L(\tilde{t}). \qquad (10)$$

The cross-size of the emitting region increases proportionally to t, the characteristic expansion time $t_c \simeq d_0/c_s \simeq 20-30$ s, where c_s is the sound speed, and the thickness changes as follows. At the beginning of expansion when the temperature is sufficiently high and Boltzmann's factor $\exp(-E_{\mathrm{eff}}/kT)$ plays no decisive role, the thickness L of the emitting layer increases, and although the temperature decreases, the radiation intensity increases. As the temperature decreases, Boltzmann's factor begins dominating and, in spite of expansion, the thickness L start decreasing and a 'collapse' of the emitting region occurs. From (10) we determine the duration of emission:

$$\tilde{t}_{\mathrm{rad}} \simeq \left[1 + \frac{L_0}{\Delta}\frac{kT_0}{E_{\mathrm{eff}} - \hbar\omega}\right]^{\frac{1}{3(\gamma-1)}}. \qquad (11)$$

For the parameters given above, $t_{\mathrm{rad}} = \tilde{t}_{\mathrm{rad}}t_l \simeq 500 \div 1000$ s. Fig. 11c shows the radiation intensity curve obtained using the model described. The outburst duration calculated is about ten minutes, which is in a good agreement with the main maximum duration observed in the light curve. Note the principal difference between the Pc2 and the main maximum: the source of the main maximum (gas ejected into the upper atmosphere) is directly seen from Earth, whereas the source of the Pc2 outburst is hidden by the limb and only the radiation scattered in the Jovian atmosphere is seen, so the main maximum intensity is appreciably higher than the Pc2 intensity. The main maximum duration is by an order of magnitude longer than the Pc2 duration. This is connected with the fact that the characteristic cooling time scale in the expanding gas increases with time by changing from a few seconds to some ten seconds at a late cooling stage.

Note that the model suggested explains easily the following observational result [50]: maximum altitudes reached by the gas ejected during different fragment falls were nearly the same, $H_{\mathrm{max}} \simeq 3000$ km. In fact, the temperature of the gas ejected is strongly dependent on the SW velocity. The initial temperature of the gas pushed out by the SW with the velocity $D \simeq 12 \div 14$ km s^{-1} somewhat exceeds T_{diss} ($T \simeq 5000 \div 7000$ K) and the maximum ejection altitude is $H_{\mathrm{max}} \simeq D^2/2g \simeq 2500 \div 3500$ km. Such a gas, which is initially transparent, becomes optically dense at late cooling stages. However, if the initial temperature of the gas ejected is significantly higher than T_{diss}, this means that the gas is being ejected from sufficiently high altitudes ($h \geqslant 150$ km over the 1 bar level) and its initial density is fairly small. At a late stage of the expansion of such a gas, when its temperature reaches $2000 - 3000$ K, its density is too small to provide the optical depth $\tau_{\mathrm{opt}} \geqslant 1$. Similarly, the gas ejected with a relatively low initial temperature ($T \leqslant 3000$ K) cools down rapidly enough to become optically transparent as well.

In 15 – 20 minutes after the cometary fragments fall, the formation of a 'plateau' is observed on the light curves. In the radiation spectrum at the stage of intensity decreasing and the 'plateau' formation (fragments K, C [46], and H [51]) some absorption lines of H_2, NH_3, CH_4, CO, and of some other species have been found. The temperature of some of these elements is of several hundred degrees, whereas the temperature of CO and NH_3 is estimated as 1500 – 3000 K. The appearance of the first group of lines is due to exponential dependence of the molecular absorption cross-section on temperature, and hence, during the cooling, the gas ejected into the upper atmosphere remains sufficiently optically thick only near the absorption maximum and becomes transparent at other wavelengths. The appearance of the secondary group lines in the spectrum and the formation of the 'plateau' seems to be caused by the heating of the atmosphere by the ejected into the upper atmosphere and falling back gas, since according to calculations [40], the fallback gas heats the atmosphere up to temperatures of some thousand degrees at altitudes of 250 – 350 km over the 1-bar level. This hypothesis is also favoured by the fact that the time of the plateau formation and of the appearance of sharp CO and NH_3 lines with a temperature of some thousand degrees well correlates with moments of the fragment impact sites crossing the limb (see Table 5). Ref. [40] assumed that the heated atmospheric layer radiates as a black body, but simple estimates show that the optical depth of such a layer is very small and the heated gas is thus a volume emitter. For this reason, despite a high temperature of the gas, the radiation intensity proves to be appreciably less than the equilibrium one and contributes insignificantly into the flux observed compared with the main maximum level. Note that at this stage emission lines corresponding to different metals were registered by spectral observations. For example, during the L and Q1 fragment fall, lines of Na, Fe, K, Ca, and Li [52] were noticed in 15 min after the impact. These lines have never been seen in the spectrum of Jupiter, which evidences for the cometary origin of metals whose lines were registered on Earth.

Some comments should be made on the light curves obtained at different wavelengths during the L fragment fall. The first feature of this curve is that the radiation intensity in the middle and far infrared range ($\lambda = 2$ μm and 10 μm [53]) corresponding to the main maximum is about an order of magnitude higher than that observed during the fall of other large fragments. Spectral observations revealed no peculiarities that somehow distinguish observational effects seen during the L fragment encounter. The most unusual were light curves obtained at wavelengths $\lambda = 0.89$ μm and 0.90 μm [45]. In these curves, approximately 16 min after the impact, at the stage of the main maximum intensity decrease, a sharp increase (nearly by three times) in the radiation flux registered is observed, followed by the equally short intensity drop. The overall duration of the outburst is about 100 s, after which the intensity decrease becomes more smooth and similar to all other light curves. At no other wavelengths (including the visible band) such outbursts were registered. It is hard to provide a reliable explanation for such a phenomenon. One possible reason could be complex non-equilibrium processes of chemical transformations in the adiabatically cooling gas of the ejection or in the atmospheric layer heated up by the falling gas. Probably, methane is the source of the observed radiation as the wavelength $\lambda = 0.89$ μm corresponds to a strong CH_4 absorption band. However, in order to verify this assumption, we should consider other light curves obtained in the visible or near-infrared region at the wavelengths corresponding to the methane absorption bands. Unfortunately, these data are not available. Note that several spike-like flashes were also observed near the main maximum for some impacts (see, for example, the R fragment light curve in Fig. 11c). These flashes are possibly of the same origin as the short intensive outburst observed during the L fragment impact.

In many papers the main maximum in the light curves is interpreted as the radiation of the atmosphere heated by the falling gas. In addition to the arguments given above favouring that this radiation mechanism determines the light curve behaviour at the stage of intensity decrease and near the 'plateau', and that the source of radiation forming the main maximum is the optically dense gas ejected into the upper atmosphere, the mechanism of the atmosphere heating by falling gas cannot explain the main maximum appearance for one more reason. As seen from Fig. 11, the time-delay t_δ between the moment of the fragment impact and the main maximum beginning is about $t_\delta \simeq 300$ s, which is typical for most fragments (except for fragments Q1 and Q2 which produced unusual light curves at the impact moments as well, see Fig. 7). The results of numerical hydrodynamic modelling show that the braking of falling gas and the subsequent atmosphere heating occur at altitudes of $h_{br} \leqslant 300$ km over the 1-bar level. Using data from Table 5, one can determine that by the moment $t = t_\delta$ after the fragment impact the heated atmospheric gas is far behind Jupiter's limb (for example, for the H fragment a distance h_{limb} between the impact site and the line of direct seeing from Earth is about 700 km $> h_{br}$). Therefore, the heated atmospheric gas cannot be a reason of the main maximum appearance in the IR light curves. Moreover, the model [40] is very sensitive to the impact site angle behind the limb, since in this case the time t_δ should correlate undoubtedly with this angle. This correlation is not found, and in contrast, in the case of the C fragment impact for which the angle of incidence behind the limb was one of the highest and $h_{limb} \geqslant 1000$ km, the time t_δ turned out to be one of the smallest (about 250 s). In Ref. [40] only the IR curve for R fragment was analyzed: among all the fragments for which the detailed light curves were obtained at different wavelengths, this fragment had a minimum angle of incidence behind the limb of about 4.8°. Therefore, the R fragment impact site emerged on the visible side of Jupiter at about the same time when a strong heating of the atmosphere by fallback gas began. It appears that the R fragment light curve was chosen in Ref. [40] just for this reason, to illustrate the model of the atmosphere heating by fallback gas.

4. Long-term atmospheric effects caused by the comet encounter

In 10 – 20 min after the impact of each of the fragments, their impact sites appeared at the limb edge (see Table 5). As Jupiter turned further, large spots appeared on the visible side at the impact sites of the fragments. The most detailed information on these spots was obtained using the Hubble Space Telescope [50]. Less detailed but longer observations were performed by ground-based observatories. Detailed spectral measurements of the impact sites were also taken from Earth. The results obtained provide the following picture of development of the comet impact traces in the atmosphere. Of 15 traces registered only five that were caused
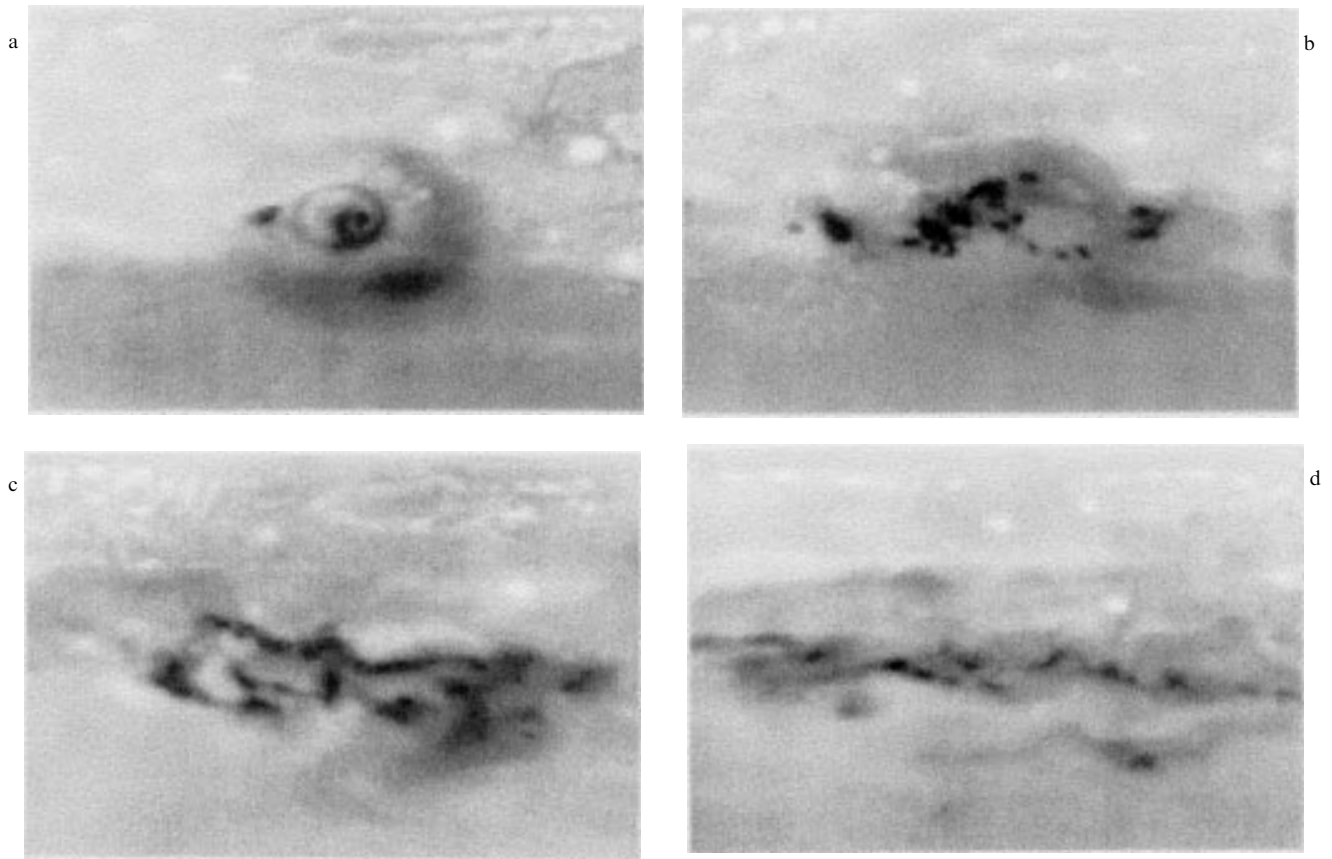
Figure 15. Images taken by the HST in the visual light. The G fragment impact site evolution is seen: (a) on July 18, 1994, (in about an hour after the impact); (b) on July 23, 1994; on August 24, 1994.

by the largest fragment impacts led to significant perturbations in the Jovian atmosphere, which were seen for a long period of time (several months). In Fig. 15 we present a series of images taken with the HST in visible light [50]. This series demonstrates the evolution of the atmospheric trace caused by the G fragment impact — one of the largest cometary fragments (a small spot to the left from the main perturbation corresponds to the impact site of a small D fragment). All images in fact relate to the initial stage of development of perturbations in the atmosphere and have clear common features and spectral peculiarities that constantly appear in images taken with various filters in the visible, IR, and UV bands. The principal feature of the spots (not only for the G fragment but in all other cases) is that they were brighter in the methane absorption bands compared with the undisturbed surface of Jupiter, and dark at all other wavelengths.

In order to understand the nature of this feature, we consider consecutively the results of spectral measurements of the impact site beginning from the moment it appeared at the limb edge. As noted at the end of the previous section, as the intensity of the main maximum in the light curve decreases, absorption lines of CO, NH_3, H_2O, etc., become dominating. This emission formed a 'plateau' at the end of main maximum, when the impact site appeared at the limb. The emission spectrum did not change significantly for a period of about 18 min until the impact spot crossed the terminator line. After the spot coming to the visible side of Jupiter, the spectrum in the visible light became forming essentially due to the solar spectrum [46]. Fig. 16 shows the results of measurements of the ratio I_J/F_S of Jupiter radiation to the incident solar radiation at three different wavelengths [39].

The longitude measured along a line connecting centres of the G and D impact sites is along the abscissa. The dash-dotted and solid lines correspond to the results obtained before and after the fragments fall. Radiation of the unperturbed atmosphere at wavelengths $\lambda = 275$ nm and 955 nm is formed by the solar light reflected from the upper cloud surface. At
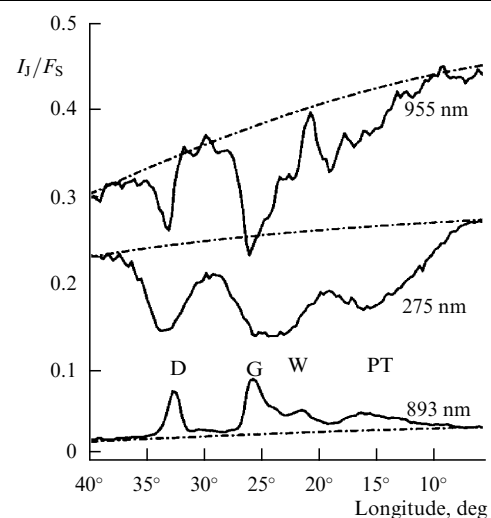
Figure 16. The longitude dependence of the ratio I_J/F_S of the radiation from Jupiter to the incident solar light for different wavelengths [39]. The D and G fragment impact sites are marked. The crossing with the ring around the G impact site center (Fig. 15a) is labelled with W, and PT marks the crossing with the moon-like trace.

$\lambda = 893$ nm, a strong absorption is observed in the Jovian atmosphere caused by the presence of methane, so emission at this wavelength is appreciably weakened. Letters D and G on this plot label the D and G fragment impact sites, respectively. Letter W marks the crossing point with a ring around the G fragment impact centre (see Fig. 15a), and symbol PT labels the crossing with a crescent-shaped trace. As seen from the plot presented, at the wavelength $\lambda = 893$ nm a significant intensity increase appears from regions corresponding to the fragment fall trace, whereas at other wavelengths the opposite picture is observed. Such a picture was seen at all wavelengths corresponding to the methane absorption bands [54], as well as in the UV spectrum.

This effect was naturally explained in Refs [39, 46, 54] as follows. In the atmospheric layer near the impact site, which is heated up both by the SW and by the ejected and fallback gas, the formation of aerosol particles begins as a result of expansion and cooling. The optical depth of the aerosol cloud formed does not exceed unity. This explains that the emission spectrum of the spot before the impact site crossing the terminator was dominated by absorption lines of different elements that appeared in the heated gas as a result of non-equilibrium chemical reactions, and after appearing on the visible side the spectrum became similar to the solar one. That the impact sites proved to be bright in the methane absorption bands evidences for the upper boundary of the aerosol cloud being higher than the atmosphere transparency boundary at any wavelength corresponding to the methane absorption lines. At wavelength $\lambda = 3.2$ μm the transparency boundary is at a level corresponding to a pressure $p \simeq 10^{-3}$ bar. As follows from calculations presented in Ref. [54], the mean size of the aerosol particles was about 0.15 μm and the particle concentration within the layer (integrated over its thickness) was approximately 2×10^8 cm^{-2}. An explanation could be given that the methane line emission increases due to the gas heating, however this feature continued to exist during subsequent several months, and the results of measurements of the temperature in the spots demonstrate that already in a few hours after the impact the spot temperature was practically indistinguishable from the outer one. For example, in five hours after the H fragment encounter the average spot temperature was found to be higher than the external one by $5.3 \div 6.4$ K [55] by comparing emission intensities of at wavelength 7.7 μm and of C_2H_6 at wavelength 12 μm. The spot temperature for different fragments was practically the same: the same time later the impact, A and H spot temperatures were 6.0 K and 5.5 K, respectively.

Now we try to answer the question whether is it possible to determine the SL9 fragments size and their penetration depth into the atmosphere based on analysis of data on the concentration of molecules that were synthesised during the fragment explosion and ejected into the upper atmosphere by a SW? During the ejection, the quench of concentrations of such molecules occurred, therefore they can be considered as a specific 'memory' of the shock processes under way in the generation region of a strong SW and, hence, may bring information on the explosion energy. We estimated above the largest fragment sizes using light curves obtained with the Galileo spacecraft. According to these estimates, the largest fragment size was about $2 \div 2.5$ km and their penetration depth was close to -150 km. According to another point of view [40], the SL9 consisted of relatively small fragments $0.4 \div 0.7$ km across and a shallow penetration from -20 km to -40 km occurred. Fragments size determination using

indirect data (abundance of explosion-synthesised molecules) provides us with a possibility to answer independently the question on the fragment size [56].

Most information on the abundance of molecules synthesised during fragment explosions was obtained during the first hours of observations of impact sites, when they appeared on Jupiter side illuminated by Sun. The observations were performed in a wide wavelength range and revealed an intensive emission of many molecules, many of which were observed in the Jovian atmosphere for the first time. What is the origin of these molecules: are they shock-chemistry synthesised or are they of the cometary origin and were brought to the planetary atmosphere by the SL9 fragment encounter? We try to answer this question using observational data. The most intensive emissions were registered in the methane bands [57] approximately half an hour later the impacts. The radiation was generated in the stratosphere at a gas pressure $p \sim 10^{-5}$ bar, which corresponds to altitudes $h \sim 250 \div 300$ km. Other carbon–hydrogen emissions, such as C_2H_2, C_2H_4, and C_2H_6, were observed [58], with mole fractions of non-saturated carbon–hydrogen species increasing by about an order of magnitude. Of the oxygen-containing compounds CO, H_2O, and OCS were observed, with CO being the main oxygen-containing compound: about 10^{14} g of CO was observed at altitudes $h \geqslant 200$ km [59], with mole fraction of the carbon monoxide being $[CO] \sim 5 \times 10^{-5}$. Of the sulfur-containing compounds H_2S, CS, CS_2, OCS, and S_2 were observed [60]. According to radio observations, $[CS] \simeq 5 \times 10^{-8}$, $p \simeq 7 \times 10^{-4}$ bar ($[OCS] \simeq 2 \times 10^{-7}$, $p \leqslant 10^{-3}$ bar). The HST measured the following relative concentrations of the sulfur-containing molecules: $[CS] : [H_2S] : [CS_2] \simeq 300 : 30 : 1$. These compounds have been observed on Jupiter for the first time and only at the sites of the largest SL9 fragment impacts (G, K–W complex). A total mass of the sulfur-containing compounds was of the order of 10^{13} g [61]. Note that all molecules considered above were not subjected to photolysis on time scales pointed at.

In the optical band, emission of metal atoms at the L and Q1 impact sites were detected, among which the most intensive lines belonged to alkaline metals Na, Li, K. The source of emission was located at altitudes $h \geqslant 250$ km ($p \leqslant 10^{-4}$ bar). According to Ref. [52], masses of atoms Na, Li, K in the aperture (2×10^7 km) were $m_{Na} \sim 10^6$ g, $m_{Li} \sim 10^5$ g, and $m_K \sim 5 \times 10^6$ g, respectively. Note that the long-term observations of the Q impact site enabled us to select the lines corresponding to at least ten molecules and atoms which have never been observed on Jupiter before [61]. Emissions from about 10^7 g of neutral and ionised metals, such as Mg II, Mg I, Si I, Fe I, and Fe II, were observed. Most of the compounds considered was at stratospheric altitudes $h \sim 200 \div 300$ km. It us remains only to understand: how did they come to these altitudes?

The observed emission of metal atoms can be explained by braking of a dust coma surrounding the cometary fragments in the atmosphere. As mentioned above, a characteristic size of dust grains in the coma of large fragments at the moment of entry into the atmosphere is of the order of one micron (smaller dust grains are charged in the magnetosphere before the encounter and are thereby captured by the Jovian magnetic field or carried away by the solar wind). The braking of grains of this size occurs just at altitudes of $200 \div 300$ km. Considering that the mass of the coma for large fragments is of the order of 10^{10} g and the total mass of the metals observed is about 10^6 g, we conclude that the coma braking in the upper

atmosphere could well explain both the observed intensity of the metal atoms emission and the appearance of metals at these altitudes.

Another possible source of such atoms could be removal of material from the fragment surface due to ablation during the entry into the atmosphere. As a result of the ablation, the mass-loss of the fragment per unit trajectory length can be estimated as

$$\frac{dm_a}{dh} \simeq \frac{\rho(h)\, v_i^2 S C_H}{Q}, \tag{12}$$

where C_H is the heat transfer coefficient (for SL9 fragments braking at altitudes under consideration we may set $C_H \simeq 0.1$) and Q is the evaporation heat of the cometary matter. For one-kilometre fragment the mass lost due to ablation at altitudes $h \geqslant 200$ km is of the order of 10^{10} g, which also can explain the observed metal atoms glowing.

However, the mechanisms considered above are not capable of explaining the appearance of a large number of *molecular* compounds at altitudes of $200 \div 300$ km, which were most likely synthesised in deeper atmospheric layers during the fragment explosion and ejected into the upper atmosphere by a shock wave. First of all, CO and S_2 belong to such compounds.

Now we describe a possible scenario of the appearance of CO and S_2 at the altitudes $200 - 300$ km. As described in detail above, the fragment explosion causes a strong shock wave to emerge, which during its propagation upwards begins accelerating. After the explosion the SW first brakes down and starts accelerating only after passing a distance of about $(2 \div 3)\, \Delta$ (depending on the explosion geometry), so little cometary matter is present in the ejected gas — the SW push up primarily the Jovian atmospheric gas. It should be noted that although the SW propagation velocity increases with approaching the point of explosion, the gas involved in such a motion cannot be ejected into the upper atmosphere since it brakes down at distances Δ ($\Delta \leqslant 70$ km), i.e. at significantly lower altitudes where the molecules discussed are located.

During the expansion of the shock-compressed gas, a quench of chemical compounds observed with the HST occurs. It is possible to determine the quench parameters using constants of the rate of chemical processes. A strong dependence of the concentration of most compounds on the initial conditions allows us to estimate the temperature, pressure and element composition of the hot gas at the moment of quench by comparing the results of thermochemical calculations with observational data.

The most complete kinetic data are available for oxygen-containing compounds [62]. At high temperatures ($T \geqslant 2000$ K) under the thermodynamic equilibrium conditions at [O] $\leqslant$ [C], practically all oxygen is bound to CO. With temperature decreasing the equilibrium concentration of water increases. The water quench occurs when reactions $CO + H_2O = H_2CO$; $H_2CO + H_2 = CH_3 + OH$; $OH + H_2 = H_2O + H$ have stopped. For example, at the pressure of 1 bar the conversion of CO into H_2O stops at 1400 K. Thermochemical calculations at T = 1400 K show that CO is the main oxygen-containing compound at [O]/[C] $\leqslant$ 1 and under a pressure of $p \leqslant 2$ bar. Much smaller amounts of other oxygen-containing compounds (first of all H_2O, CO_2, OH, and OCS) are present in such a gas.

Emission of H_2O was discovered during the fall of largest fragments only, with [H_2O] $\simeq 10^{-7}$ for the G fragment. Thermochemical calculations data agree with these observations under a pressure of $p \simeq 0.3 \div 3$ bar and [O]/[C] = $0.03 \div 0.5$. The value of [O]/[C] $\leqslant$ 0.5 is confirmed not only by a negligible amount of water detected, but also by the fact that at [O]/[C] $\geqslant$ 0.5 a strong decrease in abundance of HCN, C_2H_2, C_2H_4, C_2H_6, CS, and CS_2 would be observed, which contradicts the observations.

By assuming the quench pressure to be of the order of 1 bar and the pressure jump in the SW to be $\delta p/p \simeq 10$, we may obtain an upper limit of the G fragment explosion depth: $h_s \simeq h$ ($p = 0, 1$ bar) — $3\Delta \simeq -50$km. Now we may estimate the G fragment explosion depth using the mass of stratospheric CO observed. If oxygen in CO were of the Jovian origin, the gas ejection would occur from a level $p \simeq 5 \div 10$ bar, since water clouds are located there†.

In fact, the G fragment penetrated down to a depth of $h_s \leqslant -250$ km and its size, according to Ref. [30], was not less than four km. Since CO emission was observed during impacts of other fragments of smaller size C, D, R, W, the oxygen in the observed CO was most likely of the cometary origin.

Considering CO as a result of a shock chemistry inside the meteor trace and taking the observed CO mass ($m_{CO} \sim 10^{14}$ g), we can find the altitudes h_{ej} from which the carbon monoxide ejection occurred. Here we assume that the SW propagates upwards along the meteor trace (although the angle of entry of the SL9 fragments into the atmosphere was approximately $45°$, the results of numerical calculations [27] confirm this assumption), so that the SW involves into motion all the cometary material which is present in the trace. Using (12) we obtain that $h_{ej} \simeq 20 - 30$ km, hence, the G fragment explosion occurred at altitudes not higher than $h_s \simeq h_{ej} - 3\Delta \simeq -120$ km. Such a penetration depth corresponds to the G fragment cross-size of about two km. For the L fragment the observed amount of carbon monoxide is about an order less and the penetration depth is of the order of -80 km.

An additional information on the SL9 fragments penetration depths is provided by data on the amount of nitrogen and carbon compounds at the impact sites. The results of thermochemical calculations are in qualitative agreement with observational data on these compounds if the quench temperature and pressure is $1000 - 1400$ K and $0.01 - 0.3$ bar, respectively. If the compounds considered were formed in a fireball (explosion region) and lifted up into the stratosphere during its floating up, then the quench pressures would be much higher, which evidences for the hypothesis that these compounds are SW ejected. Therefore the saturated carbon–hydrogen compounds were most likely ejected into the planetary stratosphere from within deep layers of the planetary atmosphere, and unsaturated ones were synthesised by shock chemistry processes. Ammonium that is present in the upper cloud layer is a good detector of the shock chemistry processes, since it transforms into N_2 and HCN in them. Molecules of NH_3 and HCN were observed at the sites of many fragment encounters. This apparently means that these fragments reached the ammonium clouds layer ($p \simeq 0.6$ bar, $h \simeq 20$ km). The condition of the gas ejection from these altitudes provides an estimate for the penetration depth h_s: $h_s \simeq -120$ km. Here we assumed that all nitrogen is of the

† According to recently published data [2] collected by Galileo, which studied the composition and structure of the Jovian atmosphere, the water clouds are absent at least at the site of the probe entrance into the atmosphere and the water abundance in the Jovian air is small (about an order of magnitude less than expected). This confirms indirectly the assumption that the observed oxygen in CO is of the cometary origin.

Jovian nature. If this is not the case, the altitude obtained gives a lower limit to the explosion depth.

Finally, at some impact sites an anomalously high abundance of sulfur S_2 was observed. According to Ref. [61], about 10^{13} g of S_2 was synthesised. The theory of quench suggests no explanation to the observed abundances of S-compounds in the parameter interval covering all possible impact variants. Assuming that the sulfur-containing compounds were synthesised during the shock wave propagation through a layer of NH_4SH clouds ($p \simeq 1.5$ bar, $h \simeq -10$ km)†, we conclude that in this case the fragment penetration depth is $h_s \simeq -180$ km and its characteristic size is $2.5 \div 3$ km.

Now we suppose that the observed sulfur is of the cometary origin. Since at the G fragment impact site the observed amount of CO is $\simeq 10^{14}$ g and of S_2 is $\simeq 10^{13}$ g, we come to the conclusion that the ratio [O]/[S] is $\simeq 20$ in the cometary matter. The penetration depth in this case is $h_s \simeq -120$ km. It is seen that the largest SL9 fragment sizes in all cases considered are of the order of $2 \div 3$ km and their initial energies are $E_0 \simeq 10^{29} - 10^{30}$ ergs. Thus, the observational data on the abundance of the impact-synthesised molecules favour a model of deep penetration of the SL9 fragments into the Jovian atmosphere and confirm indirectly the size and energy estimates for the largest fragments obtained in Section 3.

We now turn to studying the dynamics of processes that determine the evolution of impact sites. Clearly, the appearances of these processes may be described using an analysis of dynamic processes in the atmosphere. The SW that arises after the destruction and explosion of a cometary fragment and moves up into the upper atmospheric layers and the fireball floating up produce intensive perturbations of the ambient medium which are capable of generating a broad spectrum of waves propagating outward the epicentre. In the general case, such perturbations may appear as acoustic waves caused by the gas compressibility, gravity waves (inertial-gravity waves) caused first of all by a joint action of gravitational and buoyancy forces, as well as Rossby waves due to the Coriolis force change on a characteristic wave scale [63]. The conditions of generation and evolution of each of these wave types were predicted in papers that had already appeared before the comet encounter with Jupiter [64 – 67]. In these papers, principal spatial-temporal characteristics of the expected atmospheric perturbations were obtained and conditions of their possible observations were formulated.

Let us consider how did the form and size of impact sites change. The space scales of characteristic formations in the zone of large fragment falls obtained in Ref. [50] are practically the same for all events detected. Thus, independently of the specific impact, in an hour and a half after it, the dark ring radius reaches about 3000 km and its expansion velocity is 450 m s^{-1} and is constant during the entire process. An extrapolation to the moment of fragment fall yields the initial perturbation radius in the atmosphere close to 500 km. The outer edge of the crescent-shaped formation is at a distance of 1200 km from the centre.

The structure of perturbations found in the images presented (see Fig. 15) was observed during several hours after the falls of large fragments. The fine structure becomes indistinguishable with time and dark spots remain at impact

sites (for images taken in the visible light) gradually stretching along the corresponding latitude. According to observations made during the first 3 – 4 days after the encounter, at the south-west part of the spot formed a dark dense core emerged and the eastern part of the spot acquired a more rarefied plume-like shape. During the subsequent month the perturbations, stretching more and more along the latitude, remained contrast; however, after that the visibility decreased appreciably, and the perturbations from individual encounters gradually merged [50]. Nevertheless, the residual perturbations at the comet encounter latitude differed from the background turbulence in the Jovian atmosphere during next several months.

The interpretation of the perturbation picture depicted above is given in Ref. [50] and can be briefly summarised as follows. The ring structures seen in the images and the core are formed by the ejected into the stratosphere material of the cometary fragment that exploded in deeper layers. Simultaneously with the cometary material, a large enough portion of gas from the Jovian atmosphere was to be ejected. According to the estimate [67], the clouds formed after the fragment impact comprised nine parts of the atmosphere and one part of the cometary material. A central homogeneous spot corresponds to the trunk of the fragment explosion products ejection, while a crescent-shaped formation and the observed radial structure of perturbations coming from the inner edge of the ring-like zone are caused by the fallback explosion products ejected into the ionosphere (at altitudes up to 3200 km from the point of explosion). The observed asymmetry of the ring-like structures and the presence of the crescent-shaped zone appear due to the tilt of the ejection from the vertical line to the surface, which in turn is caused by an inclined entrance of the cometary fragments into the atmosphere. The authors in Ref. [50] admit that the ejection core and the rarefied cometary material falling back from the stratosphere along the periphery of the perturbed zone are localised at substantially different altitudes, with the rarefied plume being located at a higher level. Following this hypothesis, the subsequent evolution of perturbations may be related to a wind advection of the cometary material in the Jovian atmosphere. In particular, the observed differences in dynamics of the diffusing ejection nucleus and the peripheral perturbations may be explained by the difference in structure and intensity of the wind fluxes at different altitudes. At the same time, development of perturbations during the first two and a half hours after explosion of the corresponding cometary fragments is, according to an analysis performed in Refs [50, 68], of a purely wave character, as was assumed before. Indeed, the detected velocity of expansion for these perturbation is the same for all large fragment encounters and, hence, very slightly depends on the energy deposit, which is characteristic for the linear wave propagation velocity that is determined by the medium properties only (non-linear effects change this rule negligibly). The wave character of dynamical structures is also confirmed by a constant in time velocity of the fronts selected. If the perturbations were caused by a transfer of particles, these velocities would notably decrease corresponding to the decrease in amplitude of the shock waves or advection waves propagating outward the epicentre. Based on these considerations, the authors of Ref. [68] conclude that the ring-like structures seen in the HST images are wave fronts expanding along the direction of the cometary material ejection into the atmosphere.

---

† The Galileo probe discovered only weak appearance of NH_4SH clouds, which seems to imply that the observed sulfur is of the cometary origin.

A comparison of the observed propagation velocities of these fronts with the results of specially performed calculations revealed no acoustic waves in the perturbation spectrum considered in Ref. [64]. Even a minimum calculated velocity for acoustic waves in the atmosphere of Jupiter proved to be 770 m s^{-1} (in the tropopause region). This exceeds significantly a maximum propagation velocity of perturbation (which turned out to be 450 m s^{-1}) relating to the inner edge of the ring-like region.

Inertial gravity waves considered in Ref. [65] by using a numerical three-dimensional five-level hydrodynamic model for the atmosphere dynamics have a velocity close to the observed one (400 m s^{-1}). In that paper, a fragment energy of order 10^{28} erg was assumed to be released within the stratosphere in the altitude interval corresponding to the pressure range of $0.01 - 0.1$ bar. Such a scenario for energy release seems unlikely and the results obtained are inconsistent with the calculations of waves in the stratosphere performed in Ref. [68]. The discrepancies obtained are explained in the latter paper by using incorrect boundary conditions at the upper atmospheric boundary introduced in Ref. [65]. In turn, from Ref. [68] it follows that the gravity waves caused by an energy release of 10^{27} ergs inside the troposphere in a more realistic range of altitudes corresponding to $0.2 - 20$ bar have a calculated velocity of 450 m s^{-1}. These waves are generated in the Jovian cloud cover layers and propagate into the stratosphere significantly increasing their amplitude. Therefore, the observed picture of perturbations, according to Ref. [68], is due to gravity-wave modulation of a cometary material cloud located in the low atmospheric layers. The authors of this hypothesis, however, point out that in their model the propagation of gravity waves over significant distances from the energy input region is possible only by assuming a nearly five-fold excess of the fraction of relatively heavy elements (such as oxygen) in the atmosphere of Jupiter compared with the fraction known presently, as well as by assuming the existence of a stable waveguide within the zone of water clouds. These assumptions on the composition and structure of the Jovian atmosphere are very serious and have not been confirmed by observations as yet. Thus, the interpretation of the observed traces of the cometary fragment encounters as clouds of a mixture of the cometary material with the Jovian atmosphere, perturbed by gravity waves and lifted up into the stratosphere from deeper layers, although does not contradict general physical concepts, has not been reliably confirmed experimentally and theoretically, which evidences for either incorrect results of numerical experiments, or an inadequate present understanding of the Jovian atmosphere composition, or an erroneous treatment of the observed traces in the atmosphere. In December 7, 1995, the Galileo probe entered dense layers of the Jovian atmosphere. It is not excluded that the data on the deep Jovian atmosphere composition in the pressure region of $1 \div 10$ bar obtained by the probe will confirm the prediction of Ref. [68] and make the researchers to address once more this elegant model†.

---

† According to preliminary data, the Galileo probe discovered no water clouds at the level $p \sim 3$ bar and, moreover, found that the fraction of heavy elements (among them oxygen is the most abundant) does not exceed twice the solar ratio [O]/[H]. If these data are confirmed by further studies, the basic assumptions of the model [67] will be violated and this model will be of historical interest only.

One may also make an assumption that the SW caused by the fragment explosion has an effect on the atmosphere. The calculations showed, however, that the SW energy under the assumed fragment braking scenario is too low to perturb the medium appreciably over the area comparable with that of the central dark spot, which is clearly seen in the images of the comet impact sites. In addition, the propagation velocity of perturbations generated by the shock wave exceeds the sound speed in the tropopause, which is about a factor of two higher than the expansion velocity for this spot [69]. Thus, both the gravity-wave and shock-wave formation mechanisms of the observed cloud cover perturbations suggest no reliable explanation for the specific trace structure, and, what is more important, show that energy required to generate perturbations on this scale is extremely large. As a result, to explain the picture observed it is necessary to put severe constraints on the structure and chemical composition of the atmosphere and the altitude of maximum energy release.

These difficulties can be overridden by assuming the hypothesis of a 'typhoon' nature of traces observed. Let us suppose that the shock wave and hot gaseous cloud lifting up from the explosion site act as a 'triggering mechanism' in developing vortex processes in the Jovian atmosphere similar to terrestrial typhoon formation. This hypothesis seems to be quite reasonable since the energy comprised in the vortex motion is much less than fragment's energy. Then, according to the theory developed in Ref. [70], let us assume that the main source of energy giving rise to a powerful atmospheric vortex is vertical thermal convection, whose intensity is well significant in the case of Jupiter. The vertical distribution of temperature in the atmosphere implies that the most intensive convective transfer occurs at the tropospheric level lying below the tropopause ($p \simeq 0.1$ bar) and extending from deep layers to the upper boundary of the clouds. A characteristic vertical scale of convective cells is then of order $h \simeq 100 \div 150$ km [72].

Now in the flow caused by the explosions action on the surrounding atmosphere we select quasi-regular large-scale structures with characteristic velocities $\langle \mathbf{v} \rangle$ and perturbations of smaller scales including turbulent convective cells. Then the equation for mean vorticity $\mathbf{w} = \mathrm{rot}\langle \mathbf{v} \rangle$ averaged over small-scale motions can be written in the form (in the Boussinesq approximation):

$$\partial_t \mathbf{w} = \mathrm{rot}(\alpha \mathbf{w}) + \nu \nabla^2 \mathbf{w}, \tag{13}$$

where ν is the turbulent viscosity coefficient, $\alpha \simeq 2\Omega l \sin \psi$ is a coefficient characterising the helicity in the turbulent convection field, $\mathbf{v}$ is the turbulent convective velocity field, Ω is the angular planetary rotation velocity, ψ is the geographical latitude, l is the initial space perturbation scale. The brackets mean the averaging over ensemble of the field realisations. Under the action of the Coriolis force the convective cells turn around the vertical axis, which provides the non-zero coefficient α. In this case, equation (13) determines the relationship between production of the large-scale horizontal vortices and circulation in the cells.

By analyzing the leading physical factors determining the formation and evolution of the trace, we distinguish three stages of its development. At the initial stage of the large-scale structure formation in the region of a large cometary fragment fall the principal perturbing factor is an intense vortex in the atmosphere appearing as a result of capture and rotation of the surrounding atmosphere by the SW and

fireball moving upwards. The subsequent evolution of this comparatively small-scale vortex is defined by its amplification due to acquiring an additional energy from convective motions in the atmosphere. The final stage of the trace formation in the atmosphere is determined by the action of the Coriolis force latitudinal gradient (β-effect) on atmospheric vortex, which attains by this time a size comparable with the Rossby radius, as well as by the action on this vortex of horizontal wind smoothing the perturbation formed within the atmosphere.

To estimate the characteristic horizontal scales of the perturbation formed at the first stage of the process, we use an asymptotic solution to equation (13) given in Ref. [70]. Close to the developing vortex structure centre it takes the form

$$\mathbf{w} = \frac{w_0}{L_\alpha} \left(0, \sin \frac{R_\alpha r}{2L_\alpha}, \; \cos \frac{R_\alpha r}{2L_\alpha} \right) \exp \left[\gamma_0 t - \frac{R_\alpha r^2}{4L_\alpha^2} \right]. \qquad (14)$$

The solution is given in cylindrical coordinates (r, ϕ, z), L_α is a characteristic scale for the mean helicity change, $R_\alpha = \alpha_0 L_\alpha / v$ is a dimensionless parameter, α_0 is an extremum value of α along the axis $r = 0$, γ_0 is the increment of the vortex intensification

$$\gamma_0 = \frac{\alpha_0^2}{4v} \left[1 - \frac{4}{R_\alpha} \right]. \qquad (15)$$

In the Jovian atmosphere two latitude zones are distinguished by the qualitatively different character of thermal convection [70]: an equatorial ($0° \leqslant \psi \leqslant 40°$) one and a middle-latitudinal ($40° \leqslant \psi \leqslant 60°$) one. The extension of the middle-latitudinal zone, which the comet impact region belongs to, is about 20° by latitude (24000 km). It seems natural to choose just this scale to estimate L_α. In Ref. [72] based on the analysis of shear and convective motion in the Jovian atmosphere, an estimate is given for the turbulent viscosity coefficient $v \sim 10^{10}$ cm^2 s^{-1}. We relate the maximum of the helicity coefficient at $r \to 0$ to an original small-scale vortex generated by the fragment explosion. Then from numerical experiment data (which are in good agreement with the results of theoretical model [41]) we obtain $l \simeq 120$ km. Using characteristic values of l, L_α and v chosen in such a way, we find a quantitative estimate for the coefficients entering equations (14) and (15): $\alpha_0 \simeq 24.4$ m s^{-1}, $R_\alpha \simeq 59.5$.

As follows from (15), the vortex may grow only provided that $R_\alpha > R_\alpha^{cr} = 4$. In our case this condition is satisfied, which implies that the shock-wave generated vortex motion in the atmosphere will increase.

The region of the vortex perturbation growth is confined within the radius $r \leqslant [v(R_\alpha - R_\alpha^{cr}) t]^{1/2}$. For the moment $t \simeq 2$ hour later the cometary fragment impact for which real measurements of the trace at the initial stage of the process are available [50], our estimates show that the perturbation expands over the area $r_0 \simeq 2000$ km across. This region corresponds, according to Ref. [70], to the typhoon 'eye' under terrestrial conditions, and in the images of the Jovian surface this region is naturally identified with the dark circle whose radius for different fragment impacts lies in the range $1800 \div 2300$ km at corresponding moments of time (see Ref. [50]). For earlier moments calculated according to equation (14) the circle radius falls within measurement errors [50], which allows us to consider the dependence (13) to be as precise as that proposed in Ref. [50], in which the observed
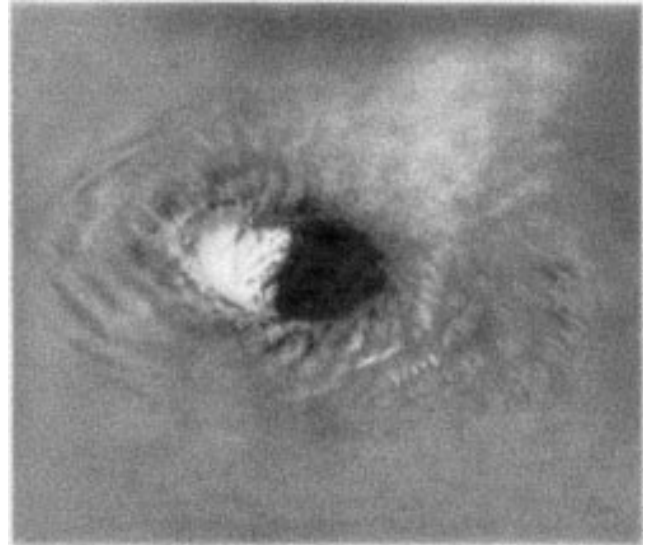

Figure 17. The 'eye' of a storm — a tropical typhoon on Earth [72].

circle radius is approximated by a simple linear dependence on time. Moreover, linear dependence does not correspond to decreasing the circle velocity with time, which is clearly seen from observations [50].

At larger distance from the centre of the perturbation the asymptotic solution (14) is not further applicable to estimate global size of the vortex perturbation. However, this estimate can now be obtained from the analysis of solution for a large-scale vortex developing against the turbulent cell background with a constant helicity coefficient α [70]. In this case the characteristic radius of perturbation is given by the relationship $r_1 = 0.5 L_\alpha / x_0$, where x_0 is the first root of the zero-order Bessel function. For the value of L_α chosen we obtain $r_1 \simeq 4800$ km, which is in good agreement with the maximum observed radius of the contrast ring-like structure seen in the images of traces from large cometary fragments (the maximum radius observed is 4700 km [50]).

The typhoon nature of the fragment fall traces is confirmed indirectly by comparing their images with a space image of the upper cloud edge in terrestrial typhoon zones (tropical storms) shown in Fig. 17 [73]. Under terrestrial conditions the typhoon 'eye' is clearly distinguished as a zone of the deep layer cloud ejection over the upper horizon of the surrounding cloud cover. In the vicinity of the 'eye', vortex is seen as spirals diverging outward the typhoon axis. These traces often look as ring-like perturbations whose centre is shifted relative to the 'eye', and the cloud cover perturbations between noticeable darker rings are of irregular character. As we see, the comet fall traces have a similar structure. The central ring that plays here the role of the 'eye' has a maximum luminosity in the spectral range corresponding to the methane. This allows us to interpret it as a zone which is characterised by lifting the material of deep atmospheric layers on to the surface of the cloud cover as told above. This interpretation is also confirmed by a red-brown colour of this region observed in the natural-colour trace images [50]. As is well known, the upper layers of the Jovian clouds consist of bright white crystals of ammonium and look light-coloured. The deeper cloud layers contain ammonium hydrosulfat with red-brown crystals. The injection of material from these layers into high altitudes forms an aerosol

layer red-brown coloured against the background of ammonium clouds.

The observed radius of the entire area spanned with perturbations during the first hours of the trace formation is $r_2 \simeq 12000$ km, which coincides with the characteristic size of the middle-latitude convection zone that we chosen from an independent analysis of thermal convection types in the Jovian atmosphere. Therefore we may consider that the vortex perturbation generated by a large cometary fragment fall and explosion expands rapidly over the entire region of convective motions of one type. The characteristic vertical scale of the typhoon vortex H at the moment of its formation is determined, according to Ref. [70], by the relationship $H \simeq h/\pi$, which in our case corresponds to $30 \div 50$ km. As follows from estimates obtained, the thickness of an atmospheric layer involved in vortex motion already at the initial stage of the process of order several hours becomes comparable with the cloud cover thickness, and its horizontal size is by more than two orders higher than the vertical perturbation scale. This must lead to an intensive vertical mixing, to velocity and temperature smoothing at horizons and destruction of quasi-stationary turbulent convective cells, which results apparently in the violation of regular energy supply to the formed large-scale vortex already by the end of the first day after its emerging, contrary to the terrestrial typhoons that acquire energy for a long time from the ocean surface lying beneath.

Note that the threshold of the large-scale vortex excitement is determined by the relationship [70] $\alpha H/v > \pi$. As according to the estimate obtained above $H \simeq 30$ km, this inequality implies that the helicity coefficient should be $\alpha > 1000$ m s^{-1}. Taking into account the relation of the coefficient α with the horizontal size of turbulent cells, we derive the condition on the size these cells must have to provide large-scale perturbation growth: $l \geqslant 400$ km. This estimate is quite realistic for the Jovian atmosphere and is confirmed by an independent estimate for turbulent viscosity. Indeed, as $v \simeq vl/3$ and the zonal flow velocity at the comet impact latitude $v \simeq 10 \div 20$ m s^{-1}, we obtain $l \simeq 1000$ km.

The vertical flow diffusion with time and appreciable excess of horizontal scales of the formed vortex over the vertical sizes allows us to study with a high accuracy the development of the process within the framework of the 'shallow water' approximation by considering the final stage of the trace evolution in the horizontal β-plane only. The large-scale vortex by that time reaches a size comparable to the Rossby–Obukhov radius [74] $R_R = c_s/2\Omega \sin \psi$, where c_s is the speed of sound at the vortex localisation horizon (for $\psi = 45°$, $R_R \simeq 6000$ km). In this situation the Coriolis force gradient along the meridian (β-effect) has a decisive effect on the subsequent vortex evolution. As a result, a sufficiently stable Rossby vortex [63] appears in the atmosphere and is then gradually diffused by zonal flows.

This stage of the process was predicted by us in Ref. [66] and was confirmed by further observations on tracing the cometary fragment impacts. We briefly repeat below the analysis of the problem performed in Ref. [66] using, however, a more accurate mathematical model.

We will depart from a two-dimensional model for the horizontal barocline atmosphere [75] taking additionally into account the zonal wind velocity fields, turbulent viscosity and heat conductivity. In this model, the basic assumption is made about smallness of the vertical scale of the process with respect to horizontal scales, and integration of hydrodynamic equations is performed over the vertical coordinate on a rotating sphere. The motion of matter is considered on a β-plane. Taking into consideration the horizontal baroclinity permits us to account for specific entropy change in the horizontal plane, which makes the description of baroclinic mechanisms of vorticity generation more correct compared with barotropic models [74, 76].

Dimensionless equations of the baroclinic atmosphere [75] with account for background winds and turbulence can now conveniently be written in a form somewhat diverging from [66]

$$\partial_t q + (\mathbf{v}_g \nabla)q = (\mathbf{v}_g \nabla)\theta - \frac{R_R}{R_f}\partial_t\left(\frac{p^2}{2}\right) + v\nabla_\perp^2 p, \qquad (16)$$

$$\partial_t\theta + (\mathbf{v}_g\nabla)\theta = \lambda\nabla^2\theta, \qquad (17)$$
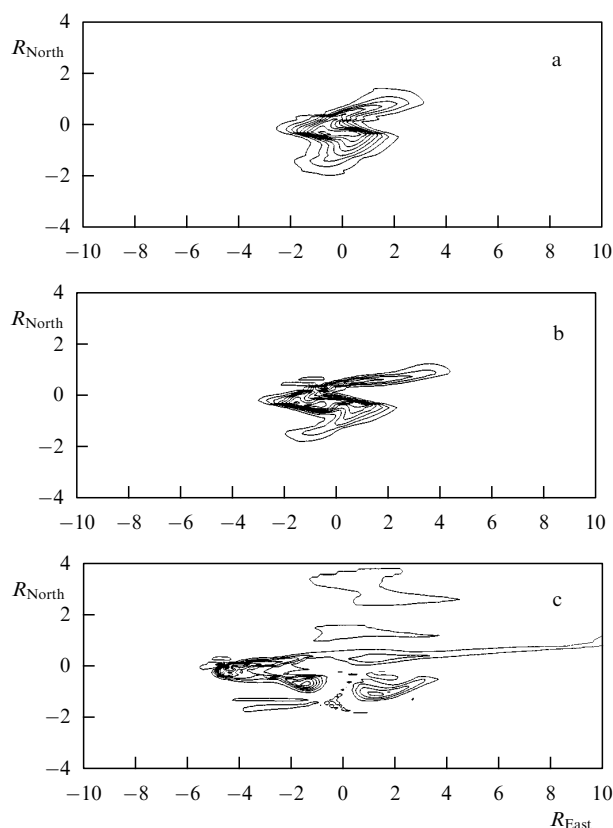
$$q = \nabla_\perp^2 p - p + \beta y, \qquad (18)$$

where $\nabla_\perp^2 = \partial_x^2 + \partial_y^2$, $\mathbf{v}_g = (\partial_y p, -\partial_x p, 0)$ is the geostrophic velocity, $\theta = p^{1/\gamma}/\rho$ is the potential temperature which is a one-valued function of entropy, p is the pressure, ρ is the density, q is a generalised vorticity, λ, v are coefficients of turbulent heat conductivity and viscosity, respectively, R_f is a characteristic size of the Coriolis parameter variation, the coordinate x is directed along the latitude and y is oriented along the meridian. The effect of zonal winds was taken into account in the initial and boundary conditions. Equations (16) – (18) were reduced to a dimensionless form as follows [75]: $(x, y) \rightarrow (R_R x, R_R y)$, $t \rightarrow tR_f/c_s$, $\rho \rightarrow \rho\rho_0 R_R/R_f$, $p \rightarrow pp_0 R_R/R_f$, $\theta \rightarrow \theta\theta_0 R_R/R_f$, where p_0, ρ_0, θ_0 are characteristic background parameters of the Jovian atmosphere at the tropopause altitudes ($p_0 \simeq 1$ bar, $\theta_0 \simeq 170$ K, $\lambda \sim v \sim 10^{10}$ cm^2 s^{-1}, $R_f \simeq 70000$ km).

Numerical calculations according to the model (16) – (18) were performed with different assumptions on the energetic of vortex perturbations formed at early stages for latitude belts of Jupiter with coordinates corresponding to impact latitudes of different fragments ($43° - 45°$ S) and wind fields typical for these latitudes.

The results of calculations showed that the Rossby vortex formation process has a threshold character. Assuming that the Rossby vortex is formed from a central part (encircled by the dark ring) of the initial large-scale vortex and taking this perturbation as an original one, we find that for an initial vortex energy of less than 10^{29} erg the Rossby vortex is not formed and the perturbation in the atmosphere decays under the action of latitude flows on a time-scale of a few days. This also permits us to estimate a lower boundary of the energy of largest SL9 fragments whose fall led to the formation of long-lived vortex structures in the Jovian atmosphere. A fragment two km across has an energy of $E_0 \simeq 10^{29}$ erg. This is in a good agreement with estimates based on the analysis of light curves obtained by the Galileo and on the content of impact-synthesised molecules in the upper atmosphere. For higher energies of the initial vortex (approximately after the first day) an anticyclonic Rossby vortex is formed from it with the final parameters only slightly depending on the initial data changing in a wide range: $0.5R_R \leqslant R_0 \leqslant R_R$, 10^{29} erg $\leqslant E_0 \leqslant 10^{30}$ erg. As the calculations show, the wind field profile at the fragment impact site affects notably the form of the Rossby vortex under formation, which apparently explains the diversity in trace forms observed several days after the comet encounter. In Fig. 18 we present the calculated fields of the potential temperature in the

vortex, corresponding to the 6th, 10th and 30th day after the cometary fragment impact. The problem initial parameters were chosen to be approximately corresponding to atmospheric parameters at the G fragment impact site. The energy content of the initial typhoon perturbation was taken to be 10^{29} erg, the initial perturbation radius was $R_0 = R_R \simeq 6000$ km. The figures presented imply that the characteristic meridional size of the vortex core nearly equals the Rossby radius on the sixth day. This coincides with the trace core size from the G fragment in the planetary surface at the corresponding moment of time [50]. Later on the Rossby vortex stretches significantly in the latitudinal direction under the action of zonal flows and the Coriolis force by keeping its meridional size nearly constant, which is noted by analyzing the images of real events. The plume deviation to the south observed for some traces not appeared in our calculations.

The estimates and numerical modelling results given above enable us to construct the following physical picture of the formation of large cometary fragment impact traces seen in the images. The traces (except for the crescent-shaped region) represent a perturbation of the upper layers of the Jovian cloud cover. A SW generated by the braking and explosion of cometary material beneath the cloud zone, as well as a fireball floating up, are the initial sources of the perturbation. This perturbation then develops into a large-scale typhoon-like atmospheric vortex, which partially accumulates the thermal atmospheric convection energy. Later, from this atmospheric vortex, a Rossby vortex is formed, however its energy proves to be insufficient for the vortex to become a super-long-lived formation like the Big Red Spot or Brown Clouds. The perturbation formed evolves with time during about a month by stretching in the latitude direction, loosing its intensity and the vortex-like individuality. Note that check calculations, in which the initial perturbation advection only by horizontal wind was taken into account, produced a significantly larger initial perturbation transfer along the latitude than that obtained in calculations with account for β-effect and that is seen in Fig. 15, which is indicative of a significant stabilising role of the Rossby vortex in the trace evolution process.
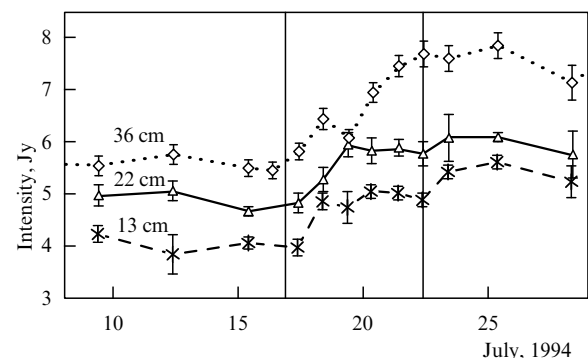
5. The Jovian magnetospheric and ionospheric response to the comet impact

Observations of the upper atmosphere and magnetosphere of Jupiter before, during, and after the SL9 encounter revealed some unexpected effects caused by the cometary fragments. First of all we should note a significant brightness increase of the Jovian radiation belt emission in decimetric band and a spectral shift of the emission into higher frequency region [77 – 80].

Observations performed at the Australian Radiotelescope (AT) and the Molonglo observatory telescope (MOST) [77, 79] (at wavelengths $\lambda = 13$ cm, 22 cm, and 36 cm) demonstrated that the Jovian radiation belt brightness started increasing in one day after the first cometary fragment impact and reached the maximum soon after the last impact. Later on, the radio flux decreased at these wavelengths on a characteristic time-scale of about 100 days, being higher by about 10% of their undisturbed value three months later. Similar results were obtained by some other observatories [78, 80]. These results turned out to be unexpected for researchers, as the absolute majority of them predicted the decimetre flux decreasing after the comet encounter.

Fig. 19 shows variations of the decimetre flux from Jupiter before, during, and after its encounter with the comet at the three wavelengths mentioned above.

An analysis of decimetre emission during impacts permits us to conclude that the emission spectrum became harder, and the source of emission, which is usually localised near the magnetic equator in the unperturbed radiation belts, expanded by shifting into the region of higher magnetic latitudes [77]. A maximum brightness increase in the radiation belts was of order 25% – 30% at $\lambda = 13$ cm and $\lambda = 22$ cm, and about 40% at $\lambda = 36$ cm.

Figure 18. The potential temperature fields after the impact of a fragment with energy $E_0 \simeq 10^{30}$ erg at different moments of time: (a) $t = 6$, (b) $t = 10$, (c) $t = 30$. The ordinate axis is directed toward the north, distances are in units of the Rossby radius, time t is in units of terrestrial days.

Figure 19. Variations of the decimetre radio flux from Jupiter before, during and after the encounter with the SL9 comet at three wavelengths: $\lambda = 13$ cm, $\lambda = 22$ cm, and $\lambda = 36$ cm [76].

The decimetre emission of Jupiter is a sum of the synchrotron radiation of relativistic electrons captured by the planetary magnetic field and thermal radiation of its upper atmosphere. The Jovian magnetic field, which at small distances (of several R_J) may be considered as possessing dipole, i.e. a purely trapping, configuration, captures fast electrons by forming the inner radiation belts, which are the main source of non-thermal emission of Jupiter in the decimetre band. Since the rotation axis of Jupiter does not coincide with the magnetic dipole axis (the angle between them is 9.6°), the radiation belts are not symmetrical.

For this reason, the magnetic field lines crossing the impact site occurred at different L-shells varying from $L \simeq 1.5$ to $L \simeq 2.5$. Here L is the maximum distance expressed in units of R_J from the Jupiter's centre to the magnetic field line. The maximum flux of synchrotron emission corresponded to $L \simeq 2$ shells. Inside these magnetic tubes, the main population of relativistic electrons has an energy of $E \simeq 10 \div 30$ MeV, and their synchrotron emission determines the radiation belts glowing in the decimetre range at wavelengths $\lambda \geqslant 15$ cm. Therefore it should be expected that the main contribution to the radiation belts perturbation will be given by those cometary fragments, whose impact site crosses the magnetic field line with parameter $L \simeq 2$. For example, the fragments A, G, K, W were among the largest [81]. Characteristic time-scales of the motion inside the Jovian magnetic fields for electrons with energies 20 MeV populating $L \simeq 1.5$ shell are as follows: the gyrofrequency of electrons is of the order of 3×10^{-6} s, the bounce-period (the time of flight between the mirror points) is 1 s, the gradient drift around Jupiter is about 3.5 days, the radiation braking is close to 40 days.

The spectral intensity of synchrotron radiation is determined by a pitch-angle distribution of relativistic electrons, their energy and the local magnetic field strength B. The spectral maximum corresponds to the frequency f_{max}:

$$f_{max} \propto E^2 B \sin \alpha, \tag{19}$$

whereas the power of emission for a single electron is found from

$$P \propto E^2 B^2 \sin^2 \alpha. \tag{20}$$

Therefore it seemed natural to predict an SL9-induced decrease in synchrotron radiation flux from radiation belts: small-size dust grains forming a coma around each fragment are charged in the Jovian magnetosphere and are captured by its magnetic field thus forming a plasma cloud. The collision of relativistic electrons with dust grains leads to either their braking, or death (due to absorption) and the subsequent decrease in the synchrotron emission flux. This effect, of course, is strongly dependent on the amount of cometary dust injected into radiation belts: it was expected that it will be sufficient to explain the observed emission flux decreasing. It turned out, however, that the cometary dust captured by the magnetosphere is insufficient to observe the effects predicted: its mass is of the order of 10^{10} g and it is transparent for fast electrons (the optical depth of the dust cloud is not higher than $\leqslant 10^{-6}$).

The observed amplification of the synchrotron emission flux requires (see (20)) either an acceleration of relativistic electrons (the acceleration of slow electrons up to relativistic energies is unlikely), or their population growth, or an increase in the pitch-angle scattering rate. In our case, all three factors possibly operate, and it us remains to understand which mechanisms make them work. Today we have no final answer to this question.

The acceleration of relativistic electrons up to higher energies leads also to the observed spectral shifting of the synchrotron radiation into higher frequency region (see (19)). In paper [82] a mechanism for fast electron acceleration was proposed — the acceleration of electrons at the front of a collisionless shock wave (CSW) generated in the upper atmosphere during the comet fragment explosion.

Although the CSW generation during fragment explosion seems quite likely, for example, during the explosion shock wave exit into the atmosphere with the subsequent transformation of the SW into a CSW, the relativistic electron acceleration seems unlikely, as it requires the simultaneous fulfillment of a number of sufficiently hard conditions [82], namely: (a) the relativistic electrons inside the CSW formation region should be present, (b) mechanisms allowing the fast electrons to cross the CSW front many times (for example, the presence of plasma turbulence at which relativistic electrons could be elastically scattered) should operate, (c) the CSW lifetime should provide the acceleration of fast electrons up to energies required.

A more likely (and more profitable energetically) acceleration mechanism is, in our opinion, a longitudinal (directed along magnetic field lines) electric field. In addition to the acceleration, the longitudinal electric field decreases the pitch-angle of electron and, hence, increases the magnetic field strength at the mirror points. Indeed, due to the first adiabatic invariant conservation $\sin^2 \alpha \propto B(\varphi)$, and the power of emission is $P \propto B^3(\varphi)$, where φ is electron's magnetic latitude. As the particle stays most time at mirror points, this too, according to (19), leads to the synchrotron emission flux enhancement and explains the shift of the radiation belts emission zone into a higher magnetic latitude region. Radial diffusion of fast electrons from upper L-shells (from peripheral magnetospheric layers) to lower L-shells also leads to particle acceleration. The first adiabatic invariant conservation, under assumption that the radial diffusion occurs faster than the radiative braking of relativistic electrons, requires $E_\perp \propto B$, $P \propto B^4$. For a dipole magnetic field $B \propto L^{-3}$, and $P \propto L^{-12}$ and to explain the observed 25% enhancement of radio emission from radiation belts a $\Delta L \simeq -2\%$ change is required. As was shown in [83], such a shift of the L-shell can be attained by increasing two times the radial diffusion coefficient. In that case, however, most synchrotron radiation flux is generated inside near-equatorial regions (since in this case the ratio $E_\perp/E_\parallel$ increases), which is in a direct contradiction with what is observed.

An increase of the pitch-angle scattering rate can also explain the results observed. It is known that the fast electron population inside radiation belts is controlled by the level of whistler turbulence, which, in turn, is excited by an anisotropic electron distribution (this distribution is anisotropic since there is a dip in the angular distribution, the loss-cone). A quasi-stationary state of the radiation belts is provided by the fact that any injection of fresh fast electrons, for example, due to the radial diffusion from upper L-shells, leads to an enhancement of the whistler turbulence [84], which, in turn, increases the pitch-angle scattering rate and leads to a portion of fast electrons entering into the loss-cone $\alpha_c \simeq (B_{eq}/B_{max})^{1/2} \sim L^{-3/2}$. Therefore any enhancement of the whistler activity inside

the radiation belts would lead to both the pitch-angle distribution broadening and precipitation of a fraction of particles (with a pitch-angle close to α_c) into the upper atmosphere. Such an enhancement may be caused, for example, by lightning discharges induced by the cometary fragment impacts. On Earth, the lightning discharges lead to fast electron precipitating from the inner radiation belts.

Fast electrons pitch-angle distribution and their aniso- tropy degree can also be perturbed by the expansion of a plasma cloud captured by the magnetosphere of Jupiter during the SL9 fragments flyby. Other mechanisms are also possible connected with the SW crossing the atmosphere boundary or with a plasma expelled by the shock wave into the upper atmosphere. Expanding inside the Jovian magnetic field, this plasma generates a current system capable of altering the pitch-angle distribution of fast electrons inside the radiation belts. An important point is that such perturba- tions lead to precipitation of a fraction of fast particles into the upper atmosphere, where they generate an artificial 'aurora' by braking. As the particles are precipitated from both end-walls of the magnetic trap, such aurora must be observed both in northern and southern hemispheres. As we already noted above, the magnetic field lines labelled with $L \simeq 1.5 \div 2.5$ are crossing the SL9 fragment impact sites, i.e. the artificial aurora are induced in the middle-latitude atmo- sphere (for polar regions $L \geqslant 6$), where they are usually absent. Remarkably, such aurora were registered during some fragment impacts.

Immediately after the K fragment encounter an X-ray outburst was observed in the northern hemisphere in the region magnetically conjugated to the impact site. The out- burst duration was about three minutes, and its energy is estimated as $10^{13} \div 10^{16}$ W [85]. In about 50 minutes after this impact, the HST registered an UV emission from the same site, with a duration of about 10 minutes [86]. Unfortunately, no observations of the K fragment during the first 50 min after its fall were performed by the HST.

One may reliably claim that the flashes registered were caused by a fragment impact that led to precipitating a fraction of electrons or ions from the magnetic field tube crossing the impact site. As X-ray and UV outbursts had different durations, they apparently were caused by different reasons. Perhaps, the short X-ray outburst was due to relativistic electron slowing down in the upper atmosphere and the X-ray emission observed is the bremsstrahlung radiation of electrons with energies $10 \div 20$ MeV, whereas the UV glowing is most likely due to precipitation of electrons of a much smaller energy about a few keV.

Observations of the Io plasma torus (IPT) brought unexpected results [87]. The IPT results from the ionisation of gas and dust which is ejected into the magnetosphere from the Jovian satellite. First the neutral gas (predominantly SO_2) is ionised by electron collisions and is captured by the Jovian magnetic field thus forming a torus-like region with enhanced concentration near Io's orbit — the IPT. A magnetic force tube with $L \simeq 5.9$ crosses the Io, so that its end-walls fall into near-polar regions of Jupiter, close to the edge of the polar aurora oval.

It was assumed initially that the SL9 fragments, by approaching Jupiter and crossing the magnetosphere, will cause noticeable perturbations in the IPT due to fresh material injection. It is easy to estimate a characteristic size a_d of the dust grains which can be captured into the Io's plasma torus. In the absence of photoeffect and secondary

electron emission, a dust grain in plasma acquires a potential† $\phi \simeq -2.5kT_e$, where k is Boltzmann's constant, T_e is the electron temperature (in the IPT $T_e \simeq 5$ eV), so that the particle charge is $Z \propto a\phi \propto aT_e$. For example, the charge of a dust grain $a_d \simeq 0.1$ μm across in the IPT is about 1000 times the electron charge. Comparing the Larmor radius of such a dust grain (the field strength inside the IPT is $B \simeq B_0/L^3$, where $B_0 \simeq 5$ G is the magnetic field strengths at the Jovian surface, $L \simeq 6$, dust gyrofrequency $\omega_{Ld} = ZeB/m_dc$) $r_{Ld} \simeq v_d/\omega_{Ld}$ with the scale of magnetic field inhomogeneity of R_J, we find that only tiny grains $a_d \ll 0.1$ μm across are captured in the IPT.

The cometary material injection into the IPT could change the IPT spectral features, in particular, the emission characteristic of the SL9 comet was expected to appear. A significant amount of the coma dust component could decrease the resistance along the magnetic force tube crossing the IPT and thus alter the current system connected with Io and closing in the ionosphere of Jupiter‡. In this connection we should notice that an artificial polar aurora has recently been observed — the Io's projection on to the ionosphere along the magnetic field lines, a result of the dissipation of longitudinal currents inside the ionosphere excited during Io's motion across the magnetic field [88]. The aurora connected with Io was observed in the IR band at the wavelength $\lambda = 3.4$ μm. Ionospheric H_3^+ ions, which are formed due to a rapid charge transfer of newly formed H_2^+ ions on the hydrogen molecules $H_2^+ + H_2 \rightarrow H_3^+ + H$, are the source of this emission. The enhancement of H_3^+ glowing evidences for either electron temperature increase in the ionosphere, or rapid particle precipitating from the magnetospheric trap. Both the processes lead to increasing the ion formation rate in the upper atmosphere. It was also expected that the IPT dust content during impacts may appear as the observed variations in the Jovian decametre radioemission (frequencies $f \simeq 20$ MHz). Note that measurements of the Jovian radioemission in the decametre range revealed no appreciable changes related to the comet impact.

The electron temperature decreasing in the plasma torus due to braking of fast electrons during collisions with charged dust grains could be another possible manifestation of interaction of the gas-dust coma with the IPT. However, the mass of dust injected into the IPT during the SL9 crossing the magnetosphere is small compared to the amount of dust ejected from Io's surface for the same period of time, so there must be no perturbations in the IPT related to the fragment comas.

Indeed, the ground-based observations in the optical band revealed no appearances of any spectral variations in the IPT both during the period of encounter and after it [87]. However, in the far UV range ($\lambda \simeq 1200 \div 1800$A) the IUE satellite discovered some increase in the IPT brightness. In this spectral band, similar luminosity variations have also been observed earlier, so their possible connection with the SL9 is not strictly established. The most unexpected results were brought by the extreme UV ($\lambda \simeq 300 \div 800$A) observa- tions of the IPT. The measurements obtained by the EUVE

---

† If no fast (above-thermal) electrons are present in plasma, the grain may become positively charged due to the secondary electron emission caused by fast particle impacts, but in this case also $\phi \simeq kT$.
‡ The Io-Jupiter current system generates the Jovian decametre emission ($f \sim 20$ MHz) — one of the most powerful radio source in the solar system. The SL9 was expected to induce the observed Jovian decametre intensity variations.
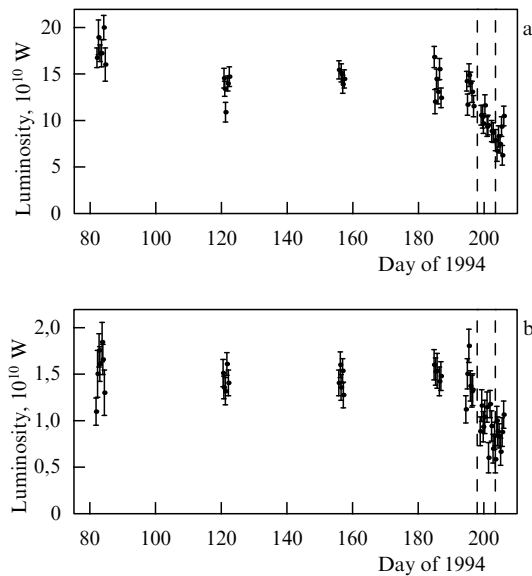
Figure 20. The extreme UV luminosity variations of the Io plasma torus (IPT) during the SL9 comet impact with Jupiter. Intensities of the IPT glowing in lines O^+ ($\lambda = 539$ A) and S^{++} ($\lambda = 680$ A) are shown as a function of time [87].

spacecraft [87] revealed an appreciable decrease in the IPT glowing (Fig. 20). The radiation intensity at the wavelength $\lambda = 539$ A (O^+ ion emission) and $\lambda = 680$ A (S^{++} ion emission) decreased by about 40% whereas the ratio of their intensities remained unchanged. Such a decrease in the IPT brightness in this spectral range was also observed in some other IPT emissions.

Clearly, a reason for such an intensity decrease cannot be the electron temperature T_e drop in the IPT only, as in that case the emission at shorter wavelengths would weaken more significantly. This is due to the emissions considered being mostly excited by electron collisions and the intensity I_λ of such an emission being very sensitive to T_e changing, since $I_\lambda \propto \exp(-E_j/T_e)$, and $E_j \gg T_e$. Note that the possible reason for the electron gas cooling in the IPT could be a shift of the magnetic field lines passing through the IPT to higher L-shells. Then adiabatic cooling of electrons occurs due to change of the volume V of the magnetic field tube: $V \propto L^4$, and $T_e \propto V^{1-\gamma} \propto L^{-8/3}$.

Probably, the reason for the Io's plasma torus brightness decrease in the extreme UV is a complex electrodynamic connection of the impact sites with the IPT. A local heating of the upper atmosphere at an impact site and the subsequent change of the ionospheric conductivity could, in principle, affect the global Jovian current system and cause some changes in the IPT; here, however, we must understand how impact sites with $L \simeq 1.5 \div 2.5$ can electrodynamically influence the IPT end-walls with $L \simeq 6$, which have no electrodynamic relation to the SL9 fragment impact sites. Possibly, the reason for the IPT brightness decreasing in the extreme UV is the same as for polar aurora anomalies observed after the comet impact. The IR measurements (the glowing of H_3^+ ion at the wavelength $\lambda = 3.4$ μm, the so-called H_3^+-aurora, was observed) performed about five days later the encounter revealed a significant brightness increase of the northern aurora compared with the unperturbed level, whereas only a slight decrease in brightness of the southern aurora was observed [89]. At the maximum brightness, the northern

aurora was about 6 – 7 times brighter than the southern one, and four times brighter its usual level. Such an anomaly has still been observed ten days after the comet impact, although a tendency to decreasing the northern aurora brightness has been noted. Such a striking reaction of the Jovian polar regions to the SL9 comet impact is not explained as yet. As of today, this question together with the question about the IPT behaviour during the period of impacts remain open.

Finally, one more interesting effect should be mentioned, which was discovered by the HST — in the near-polar southern region, during the P2 fragment fly to Jupiter (about an hour before the collision), a blinking UV aurora was observed. During about 40 min the brightness of glowing diminished from 40 kR to 5 kR, then increased again up to about 40 kR and decreased once more down to 15 kR [86, 90]. This effect clearly demonstrates the interaction of the fragment's coma with the magnetosphere of Jupiter, which leads to precipitation of fast particles from the magnetospheric trap into the upper atmosphere and generating an artificial 'polar aurora'.

Thus, the SL9 demonstrated a considerable diversity of magnetospheric and ionospheric effects, most of which is still to be explained. Contrary to the atmospheric effects caused by the cometary fragment impacts, the magnetospheric and ionospheric effects have not yet been explained even at a qualitative level. We hope this is the matter of near future.

6. Conclusions

In this review, an attempt is made to generalise, describe from unified positions the most impressive results obtained during the SL9 comet impact with Jupiter in July 1994. The main attention was given to the observational data that were reliably confirmed by many independent observers. Relatively little attention was given to 'weak' effects, the presence of which itself is not strictly established as yet (although this may be possible in future with further processing the huge amount of observational data taken in July 1994). For example, such effects include the light echo from Jovian satellites during the SL9 fragment encounters, variations of the decametre emission, or a seismic activity excitation during the encounter process. In the review we restricted ourselves to mentioning these effects only briefly, practically without discussing them in detail.

At the same time, there are some effects induced by the comet impact, whose reason is not ultimately understood. These include practically all magnetospheric effects of the impact: the increase in brightness of the radiation belts in the decimetre band, the excitation of the blinking UV aurora, outbursts of UV and X-ray emission during the K fragment impact, the enhancement of auroral activity in the northern hemisphere and its decrease in the southern hemisphere after all fragment impacts, the enhancement of the IR aurora, the brightness decrease of the plasma torus of Io in the extreme UV, and some other effects. This is partially connected with an exclusive diversity and complexity of processes underlying these effects. In this case we tried to present the most reliable and interesting observational data and to give their modern interpretation, if it exists.

The most well-studied, in out opinion, are processes of the cometary fragment entrance into the atmosphere, their braking, fragmentation, and subsequent explosion. The interpretation proposed in this review for light curves taken

by the Galileo, HST, and some ground-based observatories provides a key to understand the details of physical processes under way during the cometary fragment impact, as well as to find the penetration depth into the atmosphere and energy of a typical fragment. The model of the explosion inside an inhomogeneous atmosphere explains the most spectacular effects of the collision. At present, the model suggested is not commonly accepted, but the authors do hope that this is only the question of time, as too much fine details of the impact it describes, which cannot be a pure coincidence. The present review by no means can be considered as the final balance, it is rather an 'intermediate finish' which is devoted to fix our current understanding of the results of the comet impact with Jupiter. Many details of this encounter are not clear as yet and the authors hope that the present work, perhaps, will stimulate these studies.

References

1. Klumov B A et al. *Usp. Fiz. Nauk* **164** 617 (1994) [*Phys. Usp.* **37** 577 (1994)]
2. Isbel D, Morse D, http://www.jpl.nasa.gov/galileo, 22 January (1996)
3. West R, Böhnhardt H (Eds) *Proc. European SL9/Jupiter Workshop February 13–15, 1995* (Garching bei München: ESO Conf. and Workshop Proc. No 52, 1995)
4. Weaver H A et al. *Science* **267** 1282 (1995)
5. Scotti J V, Melosh H J *Nature* (London) **365** 731 (1993)
6. Hahn J M, Rettig T W *Geophys. Res. Lett.*, in press
7. Sekanina Z, in Ref. [3] p. 43
8. Shul'man L M *Yadra Komet* (Cometary Nuclei) (Moscow: Nauka, 1987)
9. Asphaug E, Benz W *Nature* (London) **370** 120 (1994)
10. Solem J C *Nature* (London) **370** 349 (1994)
11. Chernova G P, Kisilev N N, Jockers K, in Ref. [3] p. 11
12. Stuwe J A, Schulz R, A'Hearn M F A, in Ref. [3] p. 17
13. Jewitt D, in Ref. [3] p.1
14. Weaver H A et al. *Science* **263** 787 (1994)
15. Waddington G *The Astronomer* **30** 135 (1993)
16. Sekanina Z, Chodas P W, Yeomans D K *Astronom. Astrophys.* **289** 607 (1994)
17. Martin T Z et al. *Science* **268** 1875 (1995)
18. Carlson R W *Geophys. Res. Lett.* **22** 1557 (1995)
19. Chapman C R et al. *Geophys. Res. Lett.* **22** 1561 (1995)
20. Beatty J K, Levy D H *Sky & Telescope* **10** 18 (1995)
21. Nicholson P D et al. *Geophys. Res. Lett.* **22** 1617 (1995)
22. Graham J R et al. *Science* **267** 1320 (1995)
23. Orton G, in Ref. [3] p.75
24. Chodas P W, Yeomans D K, e-mail: sl9exploders@astro.umd.edu, (1994), *Bull. Amer. Astron. Soc.* **26** 1569 (1994)
25. Ahrens T J, Takata T, O'Keefe J D, Orton G S *Geophys. Res. Lett.* **21** 1087 (1994)
26. Takata T et al. *Icarus* **109** 3 (1994)
27. Boslough M B et al. *Geophys. Res. Lett.* **21** 1555 (1994)
28. Mac Low M M, Zahnle K *Astrophys. J.* **434** L33 1995
29. Zahnle K, Mac Low M-M *Icarus* **108** 1 (1994)
30. Gryaznov V K et al. *Earth Moon Planets* **66** 99 (1994)
31. Ivlev A V, Fortov V E, Klumov B A *Pis'ma ZhETP* **60** 481 (1994) [*JETP Lett.* **60** 491 (1994)]
32. Ivlev A V, Klumov B A, Fortov V E *Pis'ma ZhETP* **61** 423 (1995) [*JETP Lett.* **61** 431 (1995)]
33. Fortov V E, Ivlev A V, Klumov B A *Pis'ma ZhETP* **62** 752 (1995) [*JETP Lett.* **62** 772 (1995)]
34. Fortov V E, Ivlev A V, Klumov B A *Icarus*, in press
35. Grigoryan S S *Kosmich. Issled.* **17** 875 (1979)
36. Crawford D A et al. *Shock Waves* **4** 47 (1994)
37. Sedov L I *Metody Podobiya i Razmernosti v Mekhanike* (Methods of Dimensions and Similarity in Mechanics) (Moscow: Gostekhizdat, 1957)
38. Zel'dovich Ya B, Raiser Yu P *Fizika Udarnykh Voln i Vysokotemperaturnykh Gidrodinamicheskikh Yavleniĭ* (Physics of Shock Waves and High Temperature Hydrodynamic Phenomena) (Moscow: Nauka, 1966)
39. West R A et al. *Science* **267** 1296 (1995)
40. Zahnle K, MacLow M M *J. Geophys. Res.* 1996, in press
41. Kompaneets A S *Dokl. Acad. Nauk SSSR* **130** 1001 (1960)
42. Raïser Yu P *Zh. Prikl. Mekh. Tekh. Fiz.* (4) 49 (1964)
43. Borunov S, Drossart P, Encrenaz Th, in Ref. [3] p. 275
44. Watanbe J, Hasegawa T, Takeuchi S, in Ref. [3] p. 135
45. Schleicher H et al. *Earth Moon Planets* **66** 13 (1994)
46. Meadows V, Crisp D, in Ref. [3] p. 239; Meadows V et al. p. 129
47. Hasegawa H, Takeuchi S, Watanabe J, in Ref. [3] p. 279
48. Lattimer J M *Proceedings of the Conference on the Formation of Planetary Systems* (1980) p. 190
49. Yamamoto T, Hasegawa H *Prog. Theor. Phys.* **58** 816 (1977)
50. Hammel H B et al. *Science* **267** 1288 (1995); Special SL9 issues of *Geophys. Res. Lett.* **22** (12, 13) (1995)
51. Herbst T M et al., in Ref. [3] p. 119
52. Roos–Serote M et al. *Geophys. Res. Lett.* **22** 1621 (1995)
53. Lagage P O et al. *Geophys. Res. Lett.* **22** 1773 (1995)
54. Moreno F et al., in Ref. [3] p. 311
55. Livengood T A et al., in Ref. [3] p. 137
56. Berezhnoi A A, Klumov B A, Fortov V E, Shevchenko V V *Pis'ma ZhETP* **63** 387 (1996) [*JETP Lett.* **63** (1996)]
57. Encrenaz Th et al., in Ref. [3] p. 225
58. West R *ESO Messenger* **77** 28 (1994)
59. Bockelee–Morvan D et al., in Ref. [3] p. 251
60. Gautier D et al., in Ref. [3] p. 257
61. Noll D et al. *Science* **267** 1307 (1995)
62. Fegley B (Jr), Lodders K *Icarus* **110** 117 (1994)
63. Gossard E *Waves in the Atmosphere* (Amsterdam: Elsevier, 1975)
64. Collins M D et al. *J. Acoust. Soc. Am.* **95** 2880 (1994)
65. Harrington J et al. *Nature* (London) **368** 525 (1994)
66. Kamenets F F, Pukhov A M, Ivanov M F, Fortov V E *Pis'ma ZhETP* **60** 383 (1994) [*JETP Lett.* **60** 393 (1994)]
67. Klumov B A et al. *Dokl. Acad. Nauk* (Russia) **337** 28 (1994)
68. Ingersoll A P, Kanamori H *Nature* (London) **374** 706 (1995)
69. Orton G et al. *Science* **267** 1277 (1995)
70. Moiseev S S et al. *DAN* **337** 28 (1994)
71. Chamberlain J *Theory of Planetary Atmospheres* (New York: Academic Press,1978)
72. Keller B S, Yavorskaya I M, in: *Aeromekhanika i Gazovaya Dinamika* (Aeromechanics and Gasdynamics) (Moscow: Nauka, 1976)
73. Nelepo B A, Grishin G A, Kienko Yu P, Koval' A D *Opticheskie Metody Sputnikovoi Gidrofiziki* (Optical Methods of Satellite Hydrophysics) (Kiev: Naukova Dumka, 1987)
74. Pedlosky J *Geophysical Fluid Dynamics* (New York: Springer, 1982)
75. Kamenets F F, Petviashvili V I, Pukhov A M *Izv. Ross. Acad. Nauk, Ser. Fiz. Atmos. Okeana* **29** 457 (1993)
76. Charney J G *Geofys. Publ.* **17** 3 (1948)
77. Dulk G A, Leblanc Y, Hunstead R W *Geophys. Res. Lett.* **22** 1789 (1995)
78. De Pater I et al. *Science* submitted, (1995)
79. Leblanc Y, Dulk G A *Geophys. Res. Lett.* **22** 1793 (1995)
80. Sukumar S *Astron. J.* **110** 1397 (1994)
81. Bolton S J, Foster R S, Waltman *Geophys. Res. Lett.* **22** 1801 (1995)
82. Brecht S H et al. *Geophys. Res. Lett.* **22** 1805 (1995)
83. Ip W H, in Ref. [3] p. 57
84. Kennel C F, Petschek H E *J. Geophys. Res.* **71** 1 (1966)
85. Waite J H et al. *J. Geophys. Res.* **99** 14799 (1994)
86. Clarke J T et al. *Science* **267** 1302 (1995)
87. McGrath et al. *Science* **267** 1313 (1995)
88. Connervey J E P et al. *Science* **262** 1035 (1993)
89. Orton G et al. *Science* **267** 1277 (1995)
90. Prange R, Engle I M, Clarke J T *Science* **267** 1317 (1995)
91. Churymov K I, Tarashchuk V P, Prokof'eva V V, in Ref [3] p.215